Design of a Highly Efficient 20 kW Inductive Power Transfer System with Improved Misalignment Performance

Shi, Wenli; Dong, Jianning; Soeiro, Thiago Batista; Riekerk, Calvin; Grazian, Francesca; Yu, Guangyao; Bauer, Pavol

DOI
10.1109/TTE.2021.3133759

Publication date
2022

Document Version
Accepted author manuscript

Published in
IEEE Transactions on Transportation Electrification

Design of a Highly Efficient 20 kW Inductive Power Transfer System with Improved Misalignment Performance

Wenli Shi, *Student Member, IEEE,* Jianning Dong, *Member, IEEE,* Thiago Batista Soeiro, *Senior Member, IEEE,* Calvin Riekerk, *Student Member, IEEE,* Francesca Grazian, *Student Member, IEEE,* Guangyao Yu, *Student Member, IEEE,* and Pavol Bauer, *Senior Member, IEEE*

***Abstract*—Due to the urgent desire for a fast, convenient and efficient battery charging technology for electric vehicle (EV) users, extensive research has been conducted into the design of high power inductive power transfer (IPT) systems. However, there is few literature that formulates the design as a multi-objective optimization (MOO) research question considering both the aligned and misaligned performances, and validates the optimal results in a full-scale prototype. This paper presents a comprehensive MOO design guideline for highly efficient IPT systems and demonstrates it by a highly efficient 20 kW IPT system with the DC-DC efficiency of 97.2% at the aligned condition and 94.1% at 150 mm lateral misalignment. This achievement is a leading power conversion efficiency metric when compared to IPT EV charging systems disseminated in today's literature. Herein, a general analytical method is proposed to compare the performances of different compensation circuits in terms of the maximum efficiency, voltage/current stresses and misalignment tolerance. A MOO method is proposed to find the optimal design of the charging pads, taking the aligned/misaligned efficiency and area/gravimetric power density as the objectives. Finally, a prototype is built according to the MOO results. The charging pad dimension and total weight including the housing material are 516*552*60 mm^3/25 kg for the transmitter and 514*562*60 mm^3/21 kg for the receiver. Correspondingly, the gravimetric, volumetric and area power density are 0.435 kW/kg, 581 kW/m^3 and 69.1 kW/m^2, respectively. The measured efficiency agrees with the anticipated value derived with the given analytical models.**

***Index Terms*—ndutive power transfer, DC-DC efficiency, high power, misalignment tolerance, multi-objective optimization.**

NOMENCLATURE

$\dot{I}_{\rm i}$, $I_{\rm i}$ Phasor of the winding current and its root mean square value.
γ_i Ratio of $L_{\rm fi}$ to $L_{\rm i}$ in a DLCC compensated IPT system.
ϕ_{12} Phase angle difference between $\dot{I}_1$ and $\dot{I}_2$.
$C_{\rm i}$ Series compensation capacitor in a SS compensated IPT system.
$C_{\rm si}$, $C_{\rm fi}$ Series and parallel compensation capacitor in a DLCC compensated IPT system.
$f_{\rm s}$, $\omega_{\rm s}$ Switching frequency and angular switching frequency.
FOM Figure of merits of a magnetic coupler, $FOM = kQ$.
$I_{\rm i,DLCC}$, $I_{\rm fi,DLCC}$ Root mean square value of the current through $L_{\rm i}$ and $L_{\rm fi}$ in a DLCC compensated IPT system.
$I_{\rm i,SS}$ Root mean square value of the current through $L_{\rm i}$ in a SS compensated IPT system.
$L_{\rm fi}$ Compensation inductor in a DLCC compensated IPT system.
$L_{\rm i}$ Self-inductance of the charging pad.
M,k Mutual inductance and coupling coefficient between charging pads.
$P_{\rm cap}$, $P_{\rm cu}$, $P_{\rm fe}$, $P_{\rm sh}$, $P_{\rm sem}$ Power losses across the capacitor, copper, ferrite core, shielding and semiconductor losses in an IPT system.
$P_{\rm out}$, P_{12} Output power and power transferred through the air gap in an IPT system.
$P_{\rm skin}$, $P_{\rm pin}$, $P_{\rm pex}$ Skin effect, internal and external proximity effect losses in the charging pad.
Q Quality factor of a charging pad.
$R_{\rm ac}$ Equivalent AC resistance of the AC link.
$R_{\rm i}$, $R_{\rm fi}$ Equivalent AC resistance of $L_{\rm i}$ and $L_{\rm fi}$.
$U_{\rm i,DLCC}$, $U_{\rm fi,DLCC}$ Root mean square value of the voltage across $C_{\rm si}$ and $C_{\rm fi}$.
$U_{\rm i,SS}$ Root mean square value of the voltage across $C_{\rm i}$.
$i_{\rm i,DLCC}$, $i_{\rm fi,DLCC}$ Current through $L_{\rm i}$ and $L_{\rm fi}$ in a DLCC compensated IPT system.
$i_{\rm i,SS}$ Winding current in a SS compensated IPT system.
$i_{\rm i}$ Winding current in an IPT system.
$u_{\rm AB}$, $u_{\rm ab}$ Input and output voltage of the AC link.
$U_{\rm dc,1}$, $U_{\rm dc,2}$ DC input voltage of the inverter stage and DC output voltage of the rectifier stage.
subscript i $i = 1, 2$ for the Tx and Rx sides of the IPT system.

This work has received funding from the Electronic Components and Systems for European Leadership Joint Undertaking under grant agreement No 876868. This Joint Undertaking receives support from the European Union's Horizon 2020 research and innovation programme and Germany, Slovakia, Netherlands, Spain, Italy.

Wenli Shi, Jianning Dong, Thiago Batista Soeiro, Calvin Riekerk, Francesca Grazian, Guangyao Yu and Pavol Bauer are with the DCE&S/EEMCS, Delft University of Technology, Delft 2624 CP, The Netherlands (w.shi-3@tudelft.nl, j.dong-4@tudelft.nl, t.batistasoeiro@tudelft.nl, c.riekerk@tudelft.nl, f.grazian@tudelft.nl, g.yu-1@tudelft.nl, p.bauer@tudelft.nl).

I. INTRODUCTION

ELECTRIC mobility undergoes rapid development due to the global awareness of CO_2 emissions and the increasing production of electricity from renewable energy sources. Electric vehicles (EVs) can provide convenient and efficient usage of renewable energy and thus help to reduce the consumption of fossil fuels. For most of the light-duty EVs, the power

capacity of the pre-installed on-board charger is less than 19.2 kW, which means the miles of range can be restored at a rate of 20-50 $\mathrm{km/h}$ [1]. The charging process will take at least 10 hours to restore a cruising range similar to that of a conventional vehicle [1]. An urgent desire emerges in a fast, efficient and convenient charging method for EV users.

As an alternative to the conductive charging method, inductive power transfer (IPT) technology was applied to the EV battery charging application [2]–[8]. IPT technology can significantly simplify the charging procedure and thus save the labor of the EV users. It is also promising to build dynamic IPT charging roads where EVs can pick up power while travelling [5], [6], [9]–[11], thereby contributing to the reduction in the requirement of the traction batteries' capacity as well as the extension of the driving range. However, the performance index of IPT systems, including the rated power, power transfer efficiency, power density and misalignment tolerance, are limited by a number of design constraints. Since the receiver (Rx) side components are mounted in the EV, the allowable space and weight of the circuit are bounded. Therefore, a high power density of the IPT system is required. According to the standards SAE J2954, the air gap in the isolating transformer ranges from 100 mm to 250 mm, and the achievable magnetic coupling between the transmitter (Tx) and the Rx pads is limited. As compensation for the low magnetic coupling, the winding currents tend to be relatively high to reach the rated power. It is reported in [12] that the major sources of the power losses are the conduction loss in the semiconductors and the power loss in the capacitors and windings, which are mostly determined by the winding current. Thus, the power efficiency of IPT systems is limited and naturally smaller than conductive chargers. To ensure a high power transmission, it is inevitable to use large pads for a high magnetic coupling. Additionally, these pads would employ litz wire with a reasonable current density and a large number of compensation capacitors connected in series and parallel to deal with the commonly high voltage and current stresses. This trend results in conflicts between the power efficiency and power density of IPT systems. Another design restriction is the spatial offset between the Tx and Rx pads. It is required in the standards SAE J2954 that the power efficiency from the grid connection to the output of the IPT system at misaligned condition should be above 80%. To alleviate the drop of the magnetic coupling due to the misalignment, the size of the charging pads should be increased, thus reducing the power density.

To tackle the aforementioned conflicts, the design of compensation circuits and charging pads plays a dominant role. Due to the low mutual coupling, capacitors connected in series and/or parallel to a coil are commonly used to compensate the self-inductance of the charging pads [13], [14]. The compensation topology can affect the power converter design. The conventional parallel compensation, for example, requires an inductor connected in series with the inverter/rectifier on the DC side, which makes it hard for the integration design of the converters [15]. Besides, the selection of the compensation topology and its tuning strategy can have a significant impact on the system performances, in terms of the maximum efficiency, optimal load characteristics, winding current stresses and capacitor voltage stresses. The compensation study for this paper focuses on the series-series (SS) and double-sided LCC (DLCC) compensations because their resonant frequency is independent of the load and coupling coefficient which requires no change of the frequency for the misaligned cases. It is presented in [16] that the power transfer efficiency of the DLCC compensated IPT system can be improved by a proper selection of the compensated inductor, while the analytical expression of the optimal design is not solved due to the complexity of the resonant circuit. Since there is no analytical method that can explicitly derive the optimal efficiency of a DLCC compensation circuit, this paper presents a general method that can analytically compare the maximum AC link efficiency of the SS and DLCC compensated IPT systems. Besides, a parametric sweep of the compensated inductor is conducted to illustrate the global performances of the DLCC compensation. The performances of the DLCC compensation and the SS compensation under aligned and misaligned conditions are derived and compared in terms of the power transfer efficiency and current/voltage stresses on the compensation components.

As reported in [17], an important figure-of-merit (FOM), $FOM = kQ$ where k is the magnetic coupling coefficient and Q is the coil quality factor, determines the maximum efficiency of an IPT system [18]. Extensive research has been conducted into both the coil topology [3], [19]–[24] and the optimization of the geometric parameters [11], [12], [15], [25], [26] for a high FOM. Various charging pad topologies have been proposed, such as circular, rectangular, double-D (DD), bipolar and DD Quadrature (DDQ) pads. To fairly evaluate the advantages of different pad topologies, the evaluation should be based on the optimal performances considering all the design variables of the charging pads [27]. In [15], a multi-objective optimization (MOO) method is proposed for the design of circular charging pads. This MOO method conducts parametric sweep within the design search space and takes the power transfer efficiency and power density as the optimizing objectives, which illustrates the conflicts between this two objectives in the form of Pareto fronts. The power transfer efficiency and power density cannot be maximized at the same time, and a trade-off has to be made according to the application scenarios. Later, this MOO method is applied to design a $50\,\mathrm{kW}$ IPT system with a DC-DC efficiency of $95.8\,\%$ at the aligned condition in [12]. It is common that there is a misalignment between the Tx and Rx pads when there is no aid-positioning devices, but the misaligned performances of IPT systems are not studied in [12], [15]. Although the misalignment is considered in the MOO method proposed in [25], the proposed optimal design is not experimentally validated. Therefore, the aim of this paper is to propose a MOO method that considers both the aligned and misaligned performances of IPT systems, and also to verify the correctness of the optimal results in a prototype that delivers a leading power conversion efficiency metric when compared to IPT EV charging systems disseminated in today's literature.

Based on the Pareto fronts analysis in [25], the circular and rectangular pads outperform the polarized pads with respect

to the power transfer efficiency under the same area-related power density. Under the condition that the area enclosed by the coil is the same, the circular coil outweighs the rectangular coil in terms of the magnetic coupling, but considering the available space in a practical application, the rectangular coil can cover a larger area and be more favorable than the circular coil instead [15]. Therefore, the rectangular configuration is selected for the design of the proposed 20 kW IPT system discussed in this paper.

The main contributions of this paper include:

1) A comprehensive MOO design guideline for highly efficient IPT systems that can transfer the rated power and maintain a high efficiency at 150 mm lateral misalignment.
2) Validation of the developed design guideline by a 20 kW IPT system delivering a leading aligned and misaligned power efficiency, and area power density.
3) A general analytical method evaluating the maximum efficiency and voltage/current stresses of a AC link using the SS or DLCC compensation.
4) A MOO design method of a rectangular coupler that considers the air gap among the coil, ferrite cores and shielding plate, and the gap between adjacent coil turns.

This paper is structured in seven parts. In Section II, a brief review of the state-of-art IPT systems used for EV battery charging is summarized. A detailed guideline on how a 20 kW IPT system is optimized in terms of the power efficiency, power density and misalignment tolerance is presented. The analysis and design of the compensation circuit, the power electronics topology and load matching method, and the charging pads are presented in Section III, IV and V, respectively. Section VI presents the developed prototype with the area power density of 69.1 kW/m^2. The experimental measurements in the designed IPT system are used to verify the accuracy of the finite element model and the power losses calculation method. The prototype can deliver a DC-DC efficiency of 97.2% under the aligned condition and a efficiency of 94.1% under 150 mm lateral misalignment, which is a record among the available reported literature for IPT systems with power capability above 20 kW. The general conclusions are summarized in Section VII.

II. Review of the State-of-Art Prototypes

The power transferred through the air gap of an IPT system P_{12} is [18]

$$P_{12} = \Re\left\{j\omega_{\mathrm{s}} M \dot{I}_1 \dot{I}_2^*\right\} = \omega_{\mathrm{s}} M I_1 I_2 \sin\phi_{12} \qquad (1)$$

where ω_s is the angular switching frequency, M is the mutual inductance between the charging pads, ϕ_{12} is the fundamental frequency's phase difference between the Tx and Rx winding current phasors $\dot{I}_1$ and $\dot{I}_2$, I_{i} is the root mean square (RMS) value of $\dot{I}_{\mathrm{i}}$ (subscript $i = 1, 2$ stands for the Tx and Rx sides of the IPT system, respectively). Eq. (1) proves that P_{12} can be augmented by increasing ω_s, M and winding currents. The reported high-power IPT systems available in the literature with rated power above 20 kW are presented in Table I, based on which their performances are illustrated in Fig. 1. It shows

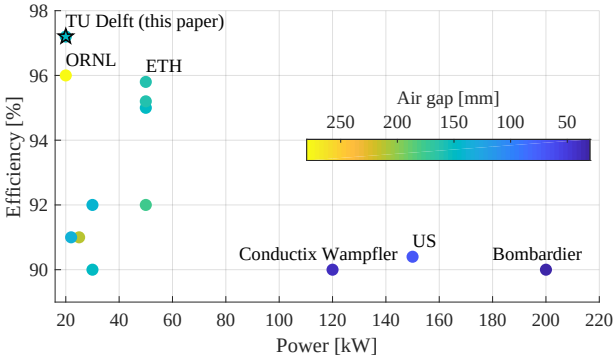

Fig. 1. Performances of the state-of-art IPT systems recorded in Table I.

a trend to reduce the air gap for a higher power. The air gap decreases from 280 mm at 20 kW [42] to 30 mm at 200 kW [1]. Increasing ω_s for a higher power is not always preferred due to the large voltage stress over the compensation capacitors and between the adjacent coil turns. Thus, the on-line electric vehicle (OLEV) prototypes developed by Korea Advanced Institute of Science and Technology (KAIST) applies 20 kHz switching frequency [43]. Due to the limit in the increment of both ω_s and M considering the area power density, it is inevitable to utilize high DC-link voltages in both the Tx and Rx sides for IPT systems with high power levels. Most of the reported prototypes in Table I have a Tx side DC-link voltage above 750 V. For example, Korea Railroad Research Institute (KRRI) applies a full-bridge resonant inverter consisting of five inverter modules and a matching transformer to reach a maximum AC voltage of 4000 V on the Tx side.

Regarding the power transfer efficiency, Table I shows that the prototypes with the efficiency above 95% mostly operate at 85 kHz, except for Oak Ridge National Laboratory (ORNL) which uses 20 kHz at a price of lower area power density. The highest power transferred via the inductive coupling is achieved by KRRI at 818 kW with 82.7% efficiency. The highest aligned efficiency reported in existing literature is 95.8% among prototypes including the non-isolated DC-DC converters by ETH Zurich, and 96% among prototypes excluding the non-isolated DC-DC converters by ORNL. It should be mentioned that Fraunhofer institute integrated the IPT system into an EV and the measured efficiency includes the whole charging system from the grid to the battery, which is 91% at the aligned condition. Regarding the misaligned efficiency, only a few of the reported prototypes conducted misaligned operation experiments in literature, and ETH Zurich realized 92% efficiency at 150 mm lateral offset which is the highest among the reported literature in Table I. Compared with the performances of the high power IPT systems in Fig. 1, this paper develops an IPT system with a higher efficiency, 97.2% at aligned condition and 94.1% at 150 mm lateral offset. The developed IPT system also delivers a higher area power density than reported 20 kW prototypes available in the literature.

TABLE I
STATE-OF-ART IPT SYSTEMS

References	Power [kW]	Year	Airgap [mm]	Tx-Rx side DC Voltage [V]	Aligned-Misaligned Efficiency [%]	Frequency [kHz]	Area Power Density [kW/m^2]
TU Delft (this paper)	20	2021	150	800-800	97.2-94.1 (150 mm)	85	69.1
KRRI [28]	818	2015	50	4000(AC)-2800	82.7-N/A	60	N/A
Bombardier [1], [29]	200	2013	30	N/A	90-N/A	N/A	N/A
University of Seoul (US) [30]	150	2016	70	800-750	90.4-N/A	60	781.2
Conductix Wampfler [29]	120	2012	40	N/A	90-N/A	20	N/A
KAIST [31]	100	2014	260	five-module 500-620	80.8-N/A	20	N/A
ETH [12], [32]	50	2016	160	800-800	95.8-92 (150 mm)	85	160
ORNL [33]	50	2020	150	3ϕ 550-580	95-88.5 (100 mm)	85	195
Zhejiang University (ZJU) [34]	50	2021	160	three-module 800-600	95.2-N/A	85	208
WAVE [35]	50	2015	178	3ϕ 480-N/A	92-N/A	23.4	N/A
Showa Aircraft [36]	30	2009	140	N/A	92-N/A	22	N/A
INTIS [37], [38]	30	2014	100	N/A	90-N/A	30	N/A
KAIST [6]	27	2011	200	N/A-550	74-N/A	20	33.7
New York University (NYU) [39]	25	2016	210	750-375	91-N/A	85	N/A
KAIST [40]	22	2015	200	N/A	71-N/A	20	27.5
Fraunhofer [41]	22	2015	136	800-800	91-89 (120 mm)	100	61.1
ORNL [42]	20	2021	280	800-420	96-N/A	22	31.9

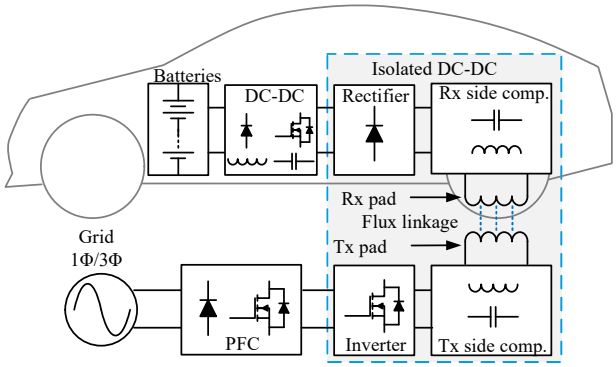

Fig. 2. Core schematics of an IPT system. The highlighted DC-DC converter is the technology of this paper scope.

III. COMPENSATION SELECTION AND DESIGN

A. Series, Parallel and LCC Compensation

The basic schematic of an IPT system is presented in Fig. 2. This circuit implements a power factor correction circuit for compliance with integration guidelines to the public AC grid (the AC-DC front-end), an isolated resonant-based DC-DC converter comprising an H-bridge inverter cascaded by a compensation circuit forming a two-stage equivalent resonant tank with the transmitter and receiver coils, and a rectifying stage (the back-end AC-DC converter). Finally, a non-isolated DC-DC converter can be used to control the charging profile across the battery of the vehicle. This final circuit can be controlled so that the battery and non-isolated DC-DC converter will behave as a controllable equivalent resistive load for the isolated DC-DC resonant converter [44]. Based on the output characteristics of the adopted compensation circuits, the optimal load matching for the maximum power transfer efficiency can be realized [45], [46].

As a loosely coupled system, capacitors, commonly connected in series and/or parallel to a charging pad, are used to compensate the self-inductance of the Tx/Rx pads so that the power transfer capability and efficiency of the system can be improved [7], [14]. The compensation is typically implemented by connecting a resonant capacitor in series or parallel to the Tx/Rx coil. For the Rx side, the parallel compensation requires a series filter inductor after the rectifying stage to limit the current through the semiconductor, resulting in a bulky secondary converter design. Considering that the space on the vehicle side is limited and the reflected impedance is not resistive, the secondary parallel compensation is not favorable in EVs charging applications where misalignment tolerance is taken into account. As a solution to this problem, the filter inductor can be replaced by a compensation inductor connected in series between the parallel resonant tank and the rectifying stage, forming an LCL compensation circuit. To further reduce the size of the compensation inductor and improve the power transfer capability, a capacitor is connected in series with the Rx coil, forming a LCC compensation circuit. Since the compensated inductor can be integrated into the charging pad [7], the compact converter design is attainable.

To ensure the high-efficiency operation of the inverter applying MOSFETs, the Tx side compensation circuits is typically designed to have the zero phase angle (ZPA) input impedance at the resonant frequency to minimize the power requirement for the inverter. Thus, the primary series and LCC compensation are widely used for EVs charging applications. In practice, the switching frequency can slightly deviate from the resonant frequency to have the output current lagging the output voltage of the inverter, allowing for its zero voltage switching (ZVS) turn-on operation, which is favourable for most MOSFET semiconductor technologies.

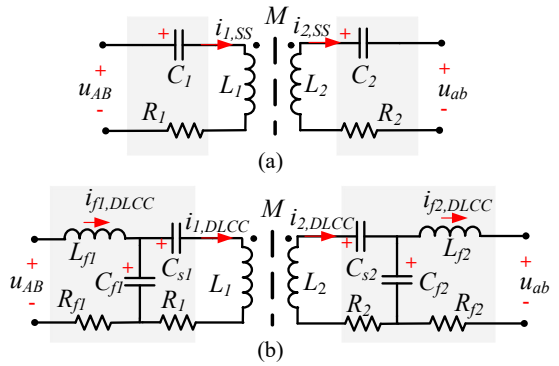

Fig. 3. AC link of IPT systems using (a) SS or (b) DLCC compensation.

Based on the above discussion, the SS and DLCC compensations are found to be suitable candidates because of their constant current output characteristics. As this paper aims to design a 20 kW IPT system with a high efficiency and good misalignment tolerance, these two compensations will be compared in terms of the maximum power transfer efficiency, the voltage stresses on capacitors and the sensitivity to the charging pads misalignment.

B. Maximum Efficiency Analysis

Previous researches have been conducted into the optimal load condition for the SS compensated IPT systems [44], [45], [47]. The analytical expressions of both the maximum efficiency and the optimal load have been solved, which provides good insights on the design of the IPT system [25]. Different from the SS compensation, the parameters of double-sided LCC compensation are designed based on the self-inductance of the charging pads as well as the DC voltage and the rated power [4], [16], [48]–[50]. Due to the consideration of misalignment tolerance and the limited space for the Rx side, the Tx pad tends to cover a larger area than that of the Rx pad. This kind of design results in an asymmetric selection of the compensation parameters, and the definition of the self-inductance of the compensation inductors L_{fi} is critical for the high efficiency operation. In [48], the expressions of the maximum efficiency and optimal load condition is derived and found to be dependent on the selection of L_{fi}. In [50], a comparison of the power efficiency is presented between a specific DLCC and a SS compensation circuits under the condition that the magnetic coupler and the compensation component equivalent series resistance are the same, but the selection of the L_{fi} for the maximum efficiency is not studied. It is found in [16] that an optimal L_{fi} exists for the maximum efficiency. However, due to the complexity of the double-sided LCC compensation circuit, the analytical expression of the optimal L_{fi} is not derived. Therefore, this paper proposes an efficiency analysis method that does not involve the specifications of the compensation circuit, and a fair comparison between the SS compensation and the double-sided LCC compensation is presented in terms of the total power losses in the AC link.

A general schematic of the AC link of an IPT system is presented in Fig. 3. The voltages across C_{i}, C_{si} and C_{fi} are $U_{\mathrm{i,SS}}$, $U_{\mathrm{i,DLCC}}$ and $U_{\mathrm{fi,DLCC}}$, respectively. The subscript $i = 1, 2$ stands for the Tx and Rx sides of the IPT system, respectively. For the SS compensation, the current through L_{i} is $I_{\mathrm{i,SS}}$. For the DLCC compensation, the currents through L_{i} and L_{fi} are $I_{\mathrm{i,DLCC}}$ and $I_{\mathrm{fi,DLCC}}$, respectively. The power transferred from the Tx side to the Rx side P_{12} can be expressed as (1). To maximize the power transfer capability, the secondary compensation should be designed to satisfy $\phi_{12} = \frac{\pi}{2}$. Otherwise, I_1 has to be increased to maintain the rated output power, leading to larger conduction losses in the Tx coil and the inverter. Therefore, the Rx side compensation design follows

$$C_2 = \frac{1}{\omega_s^2 L_2} \tag{2}$$

$$C_{\mathrm{s2}} = \frac{1}{\omega_s^2 (L_2 - L_{\mathrm{f2}})}, C_{\mathrm{f2}} = \frac{1}{\omega_s^2 L_{\mathrm{f2}}} \tag{3}$$

When the Rx side resonant circuit satisfies (2) or (3), the Rx side winding current is in phase with the Rx side induced voltage produced by the Tx side winding current. Thus, $\phi_{12} = \frac{\pi}{2}$ is guaranteed in both the SS and DLCC compensation presented in Fig. 3. From (1), one can obtain

$$I_1 I_2 = \frac{P_{12}}{\omega_{\mathrm{s}} M} \tag{4}$$

Meanwhile, the Rx side can always have a resistive reflected impedance in the Tx side, thus simplifying the Tx side compensation design for ZPA operation of the inverter. The Tx side compensation design follows

$$C_1 = \frac{1}{\omega_s^2 L_1} \tag{5}$$

$$C_{\mathrm{s1}} = \frac{1}{\omega_s^2 (L_1 - L_{\mathrm{f1}})}, C_{\mathrm{f1}} = \frac{1}{\omega_s^2 L_{\mathrm{f1}}} \tag{6}$$

To study the power losses in the AC link, the equivalent AC resistance R_{i} is assumed to be connected in series to L_{i}. When the IPT system applies SS compensation as (2) and (5), the power losses within the AC link $P_{\mathrm{loss,SS}}$ can be calculated as

$$P_{\mathrm{loss,SS}} = I_{1,\mathrm{SS}}^2 R_1 + I_{2,\mathrm{SS}}^2 R_2 \tag{7}$$

I_{i} and R_{i} are both positive-valued. Based on (7) and (4), one can get

$$P_{\mathrm{loss,SS}} \geq \underbrace{2 I_{1,\mathrm{SS}} I_{2,\mathrm{SS}} \sqrt{R_1 R_2}}_{2\frac{P_{12}}{\omega_{\mathrm{s}} M}\sqrt{R_1 R_2}} \tag{8}$$

The equality of (8) is attained when $I_{1,\mathrm{SS}}\sqrt{R_1} = I_{2,\mathrm{SS}}\sqrt{R_2}$, implying that the maximum efficiency is achieved close to the operating point where the power losses in the Tx and Rx sides are balanced.

The equivalent AC resistance R_{fi} is assumed to be connected in series to L_{fi} that is the self-inductance of the compensated inductors. When the IPT system applies DLCC compensation as (3) and (6), the power losses within the AC link $P_{\mathrm{loss,DLCC}}$ can be calculated as

$$P_{\text{loss,DLCC}} = I_{1,\text{DLCC}}^2 R_1 + I_{2,\text{DLCC}}^2 R_2 + I_{\text{f1,DLCC}}^2 R_{\text{f1}} + I_{\text{f2,DLCC}}^2 R_{\text{f2}} \tag{9}$$

Similar to (8), one can obtain

$$P_{\text{loss,DLCC}} \geq \underbrace{2 I_{1,\text{DLCC}} I_{2,\text{DLCC}} \sqrt{R_1 R_2}}_{2\frac{P_{12}}{\omega_s M}\sqrt{R_1 R_2}} + 2 I_{\text{f1,DLCC}} I_{\text{f2,DLCC}} \sqrt{R_{\text{f1}} R_{\text{f2}}} \tag{10}$$

The equality of (10) is attained when $I_{1,\text{DLCC}}\sqrt{R_1} = I_{2,\text{DLCC}}\sqrt{R_2}$ and $I_{\text{f1,DLCC}}\sqrt{R_{\text{f1}}} = I_{\text{f2,DLCC}}\sqrt{R_{\text{f2}}}$, suggesting that the maximum efficiency is realized close to the operation point where the power losses in the Tx and Rx sides are balanced.

It can be concluded by (8) and (10) that the minimal value of $P_{\text{loss,SS}}$ is smaller than that of $P_{\text{loss,LCC}}$ when P_{12} is fixed. A specific case is presented in [50] where the same magnetic coupler and the same compensation component equivalent series resistance are applied to a SS and a DLCC circuits, and the SS circuit is found to be more efficient than the DLCC.

C. Comparison of SS and DLCC Compensation

As the power of IPT systems increases, the current stresses over the coils and the voltage stresses over the capacitors are essential issues to be considered. To avoid thermal issues by too high current density through the transformer's winding, the litz wire with a large number of strands should be selected. The increment of the outer diameter of the litz wire constrains the minimal gap between the adjacent coil turns, and a relatively large pad size is designed. The rated voltage over the compensated capacitors could be above 10 kV which is far higher than the maximum AC voltage of one single off-shelf commercial film capacitor for 85 kHz applications. It is common to connect a large number of single capacitor units in series to distribute the voltage stress, posing a challenge in the integration design of the AC link.

To tackle these issues, one of the solutions is to decrease the winding current, which can be done by increasing the mutual coupling or the switching frequency as proved in (1). The coupling can be increased by reducing the air gap like the 120 kW prototype of Conductix Wampfler in Table I, or by increasing the number of turns of the coil, which leads to a smaller turn gap and a higher voltage stress over the capacitors. The limited gap between coil turns could also bring forward insulation problems and the increased thickness of the litz wire wrapper should be taken into account. In IPT systems applying elongated Tx coils like on-line electric vehicles [40], [43], [51], the voltage between adjacent coil turns can be too large owing to the equivalent inductance of each turn and the high Tx side current. Thus, the operation frequency was selected to be 20 kHz at the price of a lower power density [43]. Regarding applying higher switching frequency, it is correct that the winding current would be lower but the voltage stress will increase because the reactance of the coil is proportional to ω_s and $\sqrt{I_1 I_2} \propto \frac{1}{\sqrt{\omega_s}}$ under fixed P_{12} according to (1). For both SS and DLCC compensated IPT system, increasing the switching frequency could demand a higher DC voltage input and output, and the selection of suitable power electronics becomes limited.

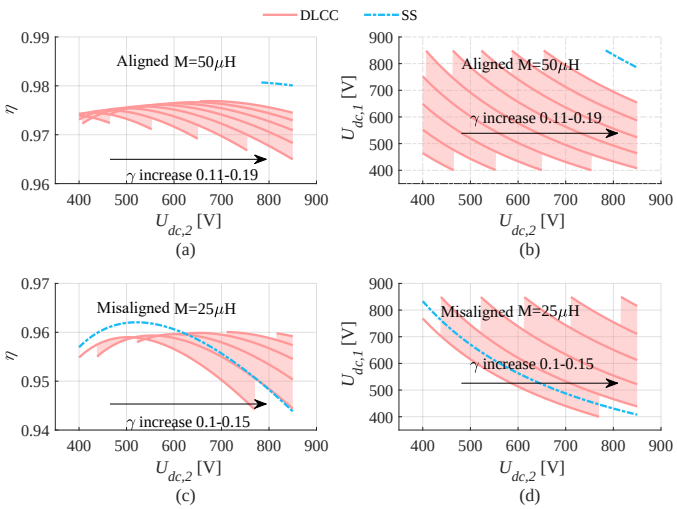

Fig. 4. Comparison of SS and DLCC compensation circuits under different Rx side DC voltage, in terms of (a) and (c) the AC link efficiency, (b) and (d) the Tx sided DC voltage requirements. At aligned condition, the mutual inductance is 50 μH as shown in (a) and (b). At misaligned condition, the mutual inductance is 25 μH as shown in (c) and (d).

The selection of compensation topology is also vital in determining the winding currents and the capacitor voltages. To have a fair comparison between the SS and DLCC compensated IPT systems, the system performances are analysed in terms of the power transfer efficiency η, DC voltage requirement $U_{\text{dc,i}}$, voltage stresses ($U_{\text{i,SS}}$, $U_{\text{i,DLCC}}$ and $U_{\text{fi,DLCC}}$) and current stresses ($I_{\text{i,SS}}$, $I_{\text{i,DLCC}}$ and $I_{\text{fi,DLCC}}$) with the DC voltage ranging from 400 V to 850 V. As the compensation performance of the DLCC compensated IPT system is dependent on the selection of L_{fi}. A parametric sweep is applied within the feasible range of L_{fi}. The ratio of L_{fi} to L_{i} is defined as γ_i, and $\gamma_1 = \gamma_2 = \gamma$ for simplicity. The self-inductance of the Tx and Rx pad are 292.3 μH and 199.6 μH, which is derived from the selected pad design in Section V. To consider the misaligned performances, the mutual inductance drops from 50 μH to 25 μH. The output power is set to be 20 kW. γ can be calculated as

$$\gamma = \sqrt{\frac{8 M U_{\text{dc,1}} U_{\text{dc,2}}}{\pi^2 \omega_s P_{\text{out}} L_1 L_2}} \tag{11}$$

Therefore, γ is investigated in the range of $0.1 - 0.19$. To analyse the efficiency of the IPT system, the quality factor Q of the charging pads and the compensation inductors are set to be 500 at 85kHz, which is close to that of the final prototype. The equivalent AC resistances can be obtained as (subscript $i = 1, 2$ stands for the Tx and Rx sides of the IPT system, respectively)

$$R_{\text{i}} = \frac{\omega_{\text{s}} L_{\text{i}}}{Q}, R_{\text{fi}} = \frac{\omega_{\text{s}} L_{\text{fi}}}{Q} \tag{12}$$

The AC link efficiency and DC voltage requirements under aligned and misaligned conditions are presented in Fig. 4. In both Fig. 4(a) and 4(c), the efficiency of the DLCC compensated IPT system is heavily dependent on the selection

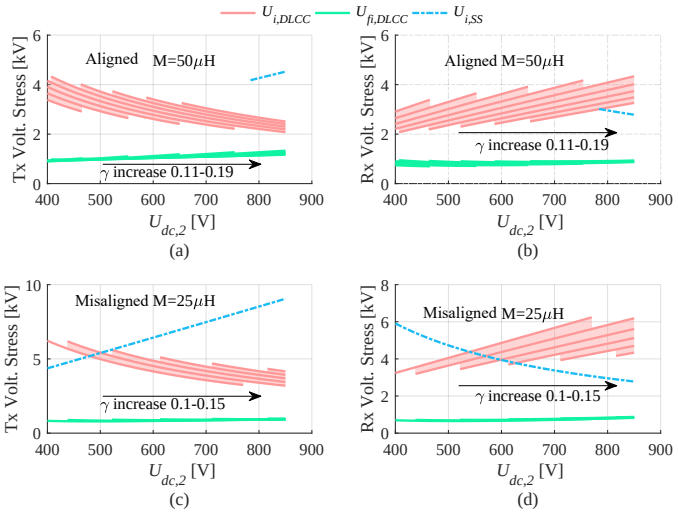

Fig. 5. Comparison of SS and DLCC compensation circuits under different Rx side DC voltage, in terms of (a) and (c) the Tx side AC voltage stresses, (b) and (d) the Rx sided AC voltage stresses. At aligned condition, the mutual inductance is 50 μH as shown in (a) and (b). At misaligned condition, the mutual inductance is 25 μH as shown in (c) and (d).

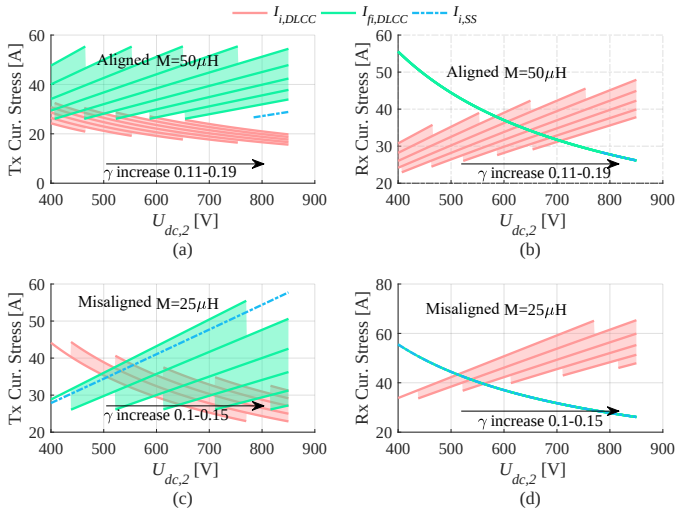

Fig. 6. Comparison of SS and DLCC compensation circuits under different Rx side DC voltage, in terms of (a) and (c) the Tx side AC current stresses, (b) and (d) the Rx sided AC current stresses. At aligned condition, the mutual inductance is 50 μH as shown in (a) and (b). At misaligned condition, the mutual inductance is 25 μH as shown in (c) and (d).

of γ, and the design with a larger value of γ is found to have a higher maximum efficiency. It is because $I_{\mathrm{fi,DLCC}}$ reduces with the rise of L_{fi}. It can also be seen that the maximum efficiency of the SS compensation is higher than that of the DLCC compensation, which verifies the analysis in Section III-B. In comparison of Fig. 4(b) and 4(d), the effective range of $U_{\mathrm{dc,i}}$ becomes narrow for SS compensation when M increases, indicating that there exists a maximum value of M for the SS compensation to deliver the rated power considering the maximum permissible DC voltage. The DLCC compensation can have a larger effective range of $U_{\mathrm{dc,i}}$ by properly selecting γ. However, if the design objective of the DLCC compensation is to maximize η, the largest value of γ should be selected and the effective range of $U_{\mathrm{dc,i}}$ is comparable to that of the SS compensation. It can be summarized that the SS and DLCC compensations have the same trend that η is high when the system can use a high DC voltage on both sides, and the SS compensation has a higher maximum efficiency than the DLCC compensation under the same M and P_{out}.

The voltage over the capacitors under aligned and misaligned conditions is depicted in Fig. 5. It can be seen that $U_{\mathrm{fi,DLCC}}$ is constantly lower than $U_{\mathrm{i,DLCC}}$ for the DLCC compensation. When comparing the SS and DLCC compensation, $U_{1,\mathrm{SS}}$ is mostly above $U_{1,\mathrm{DLCC}}$ and the difference increases when $U_{\mathrm{dc},1}$ rises as shown in Fig. 5(a) and 5(c). The trend is reversed for the Rx side as presented in Fig. 5(b) and 5(d). $I_{2,\mathrm{DLCC}}$, $I_{\mathrm{f2,DLCC}}$ and $I_{2,\mathrm{SS}}$ can be expressed as

$$\begin{cases} I_{2,\mathrm{DLCC}} = \dfrac{2\sqrt{2}U_{\mathrm{dc},2}}{\pi\omega_{\mathrm{s}}L_{\mathrm{fi}}} \\ I_{2,\mathrm{SS}} = I_{\mathrm{f2,DLCC}} = \dfrac{\pi P_{\mathrm{out}}}{2\sqrt{2}U_{\mathrm{dc},2}} \end{cases} \tag{13}$$

It is proved by (13) that $I_{2,\mathrm{DLCC}}$ increases but $I_{2,\mathrm{SS}}$ decreases as a higher $U_{\mathrm{dc},2}$ is applied. Besides, the reactance of C_{s2} is close to that of C_2 because γ is small. Thus, the Rx side voltage stress of DLCC compensation is generally higher than that of the SS compensation, especially when $U_{\mathrm{dc},2}$ is high and M is low as indicated in Fig. 5(d). As the Rx side has limited space, reducing the voltage stress on the Rx side is of higher priority to the Tx side, which makes the SS compensation more advantageous.

The current through both windings and the compensation inductors under aligned and misaligned conditions are presented in Fig. 6. It shows that the same side currents of the DLCC compensation cannot be reduced at the same time, which can be explained by (13). For the Tx side current stresses, the SS compensation presents better performances under the aligned condition as illustrated in Fig. 6(a) where $I_{1,\mathrm{SS}}$ is below the region covered by $I_{\mathrm{f1,DLCC}}$. However, the Tx side of the DLCC tends to have a lower current stress under the misaligned condition as shown in Fig. 6(c). Regarding the Rx side current stresses, the SS compensation is always better than that of the DLCC within the effective region of $U_{\mathrm{dc},2}$. As per Fig. 6(b) and 6(d), $I_{2,\mathrm{DLCC}}$ is considerably larger than $I_{\mathrm{f2,DLCC}}$ and $I_{2,\mathrm{SS}}$ when a high $U_{\mathrm{dc},2}$ is applied. It can be found that the DLCC compensation is more advantageous in avoiding high Tx side current stresses under misaligned condition. By contrast, the SS compensation holds an obviously lower current stress in the Rx side under both aligned and misaligned condition, which is more favourable in EV charging applications.

IV. System Topology and Load Matching Method

Given the mutual coupling constant, the maximum efficiency is determined by the load condition as discussed in Section III. The load matching can be realized by applying a semi-active rectifier [44] or an active rectifier [52]. By changing the phase-shift angle of the active rectifier, the amplitude and the phase of the load impedance are controlled

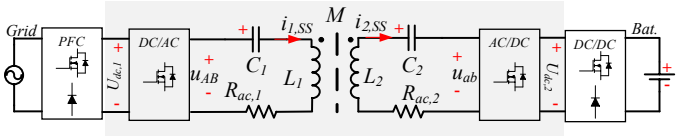

Fig. 7. IPT system overview for battery charging applications.

separately [52], which is not suitable for high power IPT applications due to the switching losses. It is more practical to apply the synchronous rectification technique on the active rectifier, which is proved to be more efficient than the diode bridge rectifier [53] but cannot effectively regulate the load. Therefore, a back-end DC-DC converter becomes necessary to change the load impedance [44]. Due to the current source output characteristics of the SS compensated IPT system, the output power regulation at a fixed battery voltage can be realized by adding a front-end DC-DC converter which will enable this functionality by adjusting the resonant circuit's input voltage. The power factor correction (PFC) stage can also provide the power regulation in a certain output voltage range by the same means, and without the need of the front-end DC-DC converter. An overview of the target IPT system is presented in Fig. 7. The advantage of applying the PFC stage and back-end DC-DC converters for the load matching and power regulation is that the resonant circuit can operate at a very narrow-band frequency close to a minimum switching losses in the inverter and rectifier stages.

The target of this paper is to design a 20 kW IPT system with $U_{\mathrm{dc,max}} = 850\mathrm{V}$. With a 3ϕ 400 V line-to-line European grid connection, the PFC can safely supply a DC voltage up to 870V with conventional two- or three-level voltage source converters, and the DC voltage requirement can be satisfied. For the Rx side, the traction battery voltage is commonly around 400V for the light-duty EVs, and a back-end buck converter becomes necessary. However, the battery voltage increases to 800V for electric buses due to the higher demand of the traction power [54]. Thus, it is also viable to remove the back-end DC-DC converter for the battery charging of electric buses. To focus more on the AC link design, the DC-DC converter is not studied in this paper. As highlighted in Fig. 7, the studied IPT system includes the inverter, AC link and rectifier.

Provided the alignment condition and ω_{s} is fixed, the AC equivalent optimal load resistance is determined as [25]

$$R_{\mathrm{L,opt}} \approx \omega_{\mathrm{s}} M \sqrt{\frac{R_{\mathrm{ac},2}}{R_{\mathrm{ac},1}}} \tag{14}$$

where $R_{\mathrm{ac,i}}$ (subscript $= 1, 2$ stands for the Tx and Rx sides of the IPT system, respectively) is the equivalent AC resistance of the AC link. To achieve the maximum system efficiency, the DC voltage $U^*_{\mathrm{dc,i}}$ under rated output power can be estimated as

$$\begin{cases} U^*_{\mathrm{dc},2} \approx \dfrac{\pi}{4}\sqrt{2P_{\mathrm{out}}\omega_{\mathrm{s}}M}\sqrt[4]{\dfrac{R_{\mathrm{ac},2}}{R_{\mathrm{ac},1}}} \\ U^*_{\mathrm{dc},1} \approx \dfrac{\pi}{4}\sqrt{2P_{\mathrm{out}}\omega_{\mathrm{s}}M}\sqrt[4]{\dfrac{R_{\mathrm{ac},1}}{R_{\mathrm{ac},2}}} \end{cases} \tag{15}$$

V. Pad Optimization Design

In IPT systems, the energy transferred from the Tx to the Rx side relies on the magnetic coupling. A high coupling is favourable to improve the efficiency in high power applications since less winding current is required as proved in (1). As a price of high coupling, the size of the charging pads may be designed larger and thus become more expensive. The misalignment tolerance can also be improved by enlarging the size of the charging pad. Considering the limited size on the EV side, a trade-off emerges among the power transfer efficiency, power density as well as misalignment tolerance. Therefore, a MOO design is recommended for the design of the charging pads.

As the effective magnetic field is within the air gap between the Tx and Rx pads, the charging pads that produce a magnetic field concentrating on one side are preferred. To achieve the single-sided magnetic field, the charging pad usually consists of litz wire coil as well as ferrite cores, and the shielding plate. The ferrite cores could enhance the coupling between the Tx and Rx pads. The shielding plate is used to reduce the magnetic stray field. To obtain the electric parameters of the charging pads, including the self-inductance, mutual inductance and equivalent AC resistance, the magnetic field has to be calculated. Due to the non-linear property of the ferrite cores and various coil topologies, the magnetic field is commonly computed through finite element (FE) models [15], [25], [55]. It is found in [25] that the circular and rectangular couplers can deliver a higher power transfer efficiency than that of the polarized couplers, DD and DDQ, at the same area power density. Considering that the rectangular coil can make full use of the allowed on-board space, the rectangular coil topology could be a more suitable candidate than the circular one. Therefore, this section focuses on the optimization design of the charging pads using rectangular coils.

A. Analytical Losses Model

To obtain the DC-DC efficiency of the IPT system, power losses should be modelled, including power converters (inverter and rectifier), capacitors and charging pads. The copper losses in the charging pads P_{cu} is composed of the DC ohmic loss P_{dc} and the AC losses due to the skin effect P_{skin}, internal P_{pin} and external P_{pex} proximity effects. According to [25], these power losses can be calculated as

$$\begin{cases} P_{\mathrm{dc,i}} + P_{\mathrm{skin,i}} = n_{\mathrm{str}} r_{\mathrm{dc}} F_{\mathrm{R}}(f_{\mathrm{s}}) \left(\dfrac{\widehat{I}_{\mathrm{i}}}{n_{\mathrm{str}}}\right)^2 L_{\mathrm{coil}} \\ P_{\mathrm{pin,i}} = n_{\mathrm{str}} r_{\mathrm{dc}} G_{\mathrm{R}}(f_{\mathrm{s}}) \dfrac{\widehat{I}_{\mathrm{i}}^2}{2\pi^2 d_{\mathrm{a}}^2} L_{\mathrm{coil}} \\ P_{\mathrm{pex,i}} = \displaystyle\sum_{k=1}^{N_{\mathrm{i}}} n_{\mathrm{str}} r_{\mathrm{dc}} G_{\mathrm{R}}(f_{\mathrm{s}}) \oint_{l_{\mathrm{k}}} \widehat{H}^2_{\mathrm{ext}}(l) dl \end{cases} \tag{16}$$

where subscript $i = 1, 2$ stands for the Tx and Rx side, $n_{\rm str}$ is the number of strands in the litz wire, $r_{\rm dc}$ is the DC resistance per unit length of a single strand, $\widehat{I}_{\rm i}$ is the peak value of the current through the coil, $N_{\rm i}$ is the number of turns of the coil, $l_{\rm k}$ is the $k_{\rm th}$ turn of the coil, $d_{\rm a}$ is the diameter of the litz wire, $H_{\rm ext}$ is the magnetic field penetrating the individual coil turns, $f_{\rm s}$ is the switching frequency, $F_{\rm R}(f_{\rm s})$ and $G_{\rm R}(f_{\rm s})$ are the frequency dependent factors [56]. The calculation of $P_{\rm pex}$ involves the geometric feature of the coil and $H_{\rm ext}$ over each individual coil turn which is derived from the FE models.

The ferrite core loss $P_{\rm fe}$ is calculated by using Steinmetz equation and integrating it over the core volume as [25]

$$P_{\rm fe,i} = \int_{V_{\rm fe,i}} k f_{\rm s}^{\alpha} \widehat{B}^{\beta} dV \tag{17}$$

where subscript $i = 1, 2$ stands for the Tx and Rx side, $V_{\rm fe}$ is the set of cores for the coil, k, α and β are the Steinmetz parameters depending on the core material. For the selected core material 3C95, the Steinmetz parameters are $k = 92.66$, $\alpha = 1.045$ and $\beta = 2.44$ for $\mathrm{W/m^3}$.

The shielding loss $P_{\rm sh}$ due to the eddy current is calculated by

$$P_{\rm sh,i} = \int_{V_{\rm sh,i}} \frac{\Re\left\{\mathbf{J} \cdot \mathbf{E}^{*}\right\}}{2} dV \tag{18}$$

where subscript $i = 1, 2$ stands for the Tx and Rx side, $V_{\rm sh}$ is the volume of the shielding plate, $\mathbf{J}$ is the induced current density amplitude on the shielding plate and $\mathbf{E}$ is the electric field at the surface boundary.

The film capacitor from TDK is selected for the 20 kW IPT system because its capacitance holds a relatively small deviation from its rated value for an operation at 85 kHz, while no critical de-rating due to hotspot caused by dielectric loss is necessary. The capacitor power loss is calculated by using the equivalent series resistance $R_{\rm cap}$ of each single unit as

$$P_{\rm cap,i} = I_{\rm i}^2 \frac{n_{\rm s,i}}{n_{\rm p,i}} R_{\rm cap} \tag{19}$$

where subscript $i = 1, 2$ stands for the Tx and Rx side, $n_{\rm s}$ and $n_{\rm p}$ are the number of capacitor units connected in series and in parallel, respectively. The selected film capacitor unit has a maximum AC voltage limit of $600\ V$. According to Fig. 5, the maximum voltage stress can be above 9 kV in RMS value at the misaligned case, which is far larger than the AC voltage limit of the capacitor unit. Thus, $n_{\rm s}$ has to be selected to ensure the voltage stress over a capacitor unit is less than its limit. Then, $n_{\rm p}$ is selected to achieve the design capacitance for the compensation according to (2) and (5). It should be noted that the total number of the capacitor units is proportional to $n_{\rm s}^2$ because of $n_{\rm p} \propto n_{\rm s}$. Therefore, it becomes important for high power applications to reduce the voltage stress for a compact design.

The ZVS operation of the inverter can be attained by keeping the input impedance slightly inductive. For the synchronous rectification stage, the ZVS operation can be realized by applying a short delay between the zero-crossing of i_2 and the switching on of the MOSFETs operating in the following next half cycle. Therefore, the switching losses

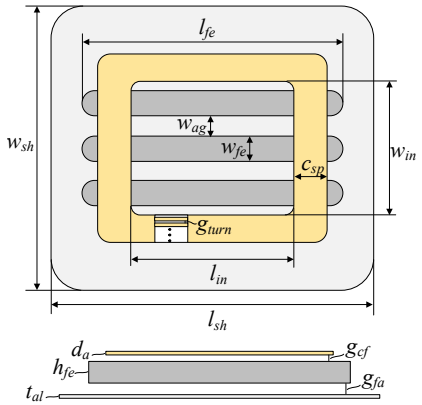

Fig. 8. Geometrical variables for the charging pad. The width of the coil spread is $c_{\rm sp} = N d_{\rm a} + (N-1) g_{\rm turn}$. To scale the length of the ferrite bar $l_{\rm fe}$ and the gap between ferrite bars $w_{\rm fe}$, they are defined as $l_{\rm fe} = l_{\rm fe,r}(l_{\rm in} + 2c_{\rm sp})/100$, $w_{\rm ag} = w_{\rm ag,r}(w_{\rm in} + 2c_{\rm sp} - n_{\rm fe} w_{\rm fe})/(100(n_{\rm fe} - 1))$, where $l_{\rm fe,r}$ and $w_{\rm ag,r}$ are the corresponding scaling factors. The shielding plate is set to have the same size with the coil, thus $l_{sh} = (l_{\rm in} + 2c_{\rm sp})$ and $w_{sh} = (w_{\rm in} + 2c_{\rm sp})$.

of the inverter and rectifier stages are negligible. The total semiconductor losses in the Tx $P_{\rm sem,1}$ and Rx sides $P_{\rm sem,2}$ can be approximated as conduction losses according to

$$P_{\rm sem,i} = I_{\rm i}^2 r_{\rm DS,on}\left(T_{\rm j}\right) \tag{20}$$

where subscript $i = 1, 2$ stands for the Tx and Rx side, $r_{\rm DS,on}$ is the equivalent on-state resistance of a single switch as a function of the junction temperature $T_{\rm j}$.

Based on the presented losses calculation method, the equivalent AC resistance of the AC link $R_{\rm ac}$ can be obtained as

$$R_{\rm ac,i} = \frac{P_{\rm cu,i} + P_{\rm fe,i} + P_{\rm sh,i} + P_{\rm cap,i} + P_{\rm sem,i}}{I_{\rm i}^2} \tag{21}$$

where subscript $i = 1, 2$ stands for the Tx and Rx side. As a vital part to improve the system power transfer efficiency, the optimal load for the SS compensated IPT system should be applied as (14). It should be noted that $R_{\rm ac,i}$ increases as the winding current becomes large, because the Steinmetz parameter β is larger than 2 according to (17) and (21). An accurate estimation of $R_{\rm L,opt}$ can only be conducted when the winding current is solved, while the winding current is determined by $R_{\rm L,opt}$. As a result, iterative steps become necessary to accurately estimate the optimal operation condition. Since $P_{\rm dc}$ is a major part of the charging pad losses [12], [15] and involves no magnetic field computation, $R_{\rm ac}$ is simplified as

$$R_{\rm ac,i} \approx \frac{P_{\rm dc,i} + P_{\rm cap,i} + P_{\rm sem,i}}{I_{\rm i}^2} \tag{22}$$

to avoid the iterative procedure and reduce the computation labour for the calculation of the optimal operation conditions.

B. FE Model and Parameters

The geometrical variables of the charging pads are illustrated in Fig. 8, where several identical ferrite bars in cuboid shape are applied. Thus, 3D FE models are required to calculate the magnetic field. To reduce the computation labour,

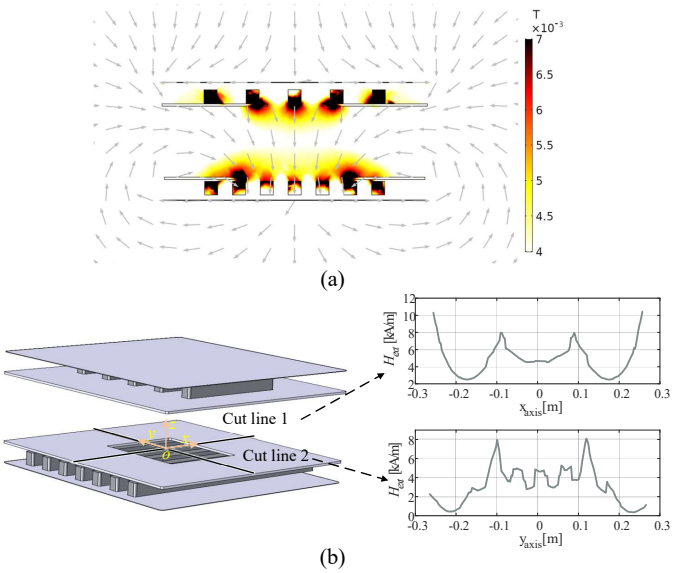

Fig. 9. Magnetic field distribution computed by a 3D FE model simulated in COMSOL 5.4, (a) B field distribution in yz plane, (b) H field distribution along cut line 1 and 2. Cut line 1 is along x axis and penetrates the center of each turn of the Tx coil. Cut line 2 is along y axis and penetrates the center of each turn of the Tx coil. The H field distribution is computed to calculate P_{pex} based on (16).

the FE model utilizes a 3D solid block with uniformed current density to model the winding as a whole instead of using pipes to model each turn of the winding. This can prevent the intensive computation load associated with the calculation of the eddy currents in the winding [25]. The diameter of the litz wire strand is selected to eliminate the skin effect. The eddy current within the winding has a very limited impact on the magnetic field distribution. Thus, the 3D FE model can deliver reliable results of the inductance and H_{ext} that is used to calculate the proximity effect loss based on (16). An example of the magnetic field computed by a 3D FE model is illustrated in Fig. 9 where the B field distribution in the yz plane and the H field distribution in the cut line 1 and 2 are illustrated. Fig. 9(b) shows that H_{ext} varies in a large range at different locations, and an obvious discontinuity emerges in the y-axis curve of H_{ext} due to the discrete deployment of the ferrite cores. Therefore, H_{ext} at multiple different points of each coil turn are computed to improve the accuracy when calculating P_{pex} based on (16).

In this FE model, the gap between the coil turns g_{turn} is included and a non-zero lower boundary is set. The advantages are 1) less proximity effect losses, 2) available space for the insulation wrapper of the litz wire, 3) lower parasitic capacitance between adjacent coil turns and 4) higher heat dissipation capability. The FE model also includes the gap between the coil and ferrites g_{cf} to consider the physical presence of the litz wire wrapper and to reduce the impact of the spikes of magnetic field concentrated at the edges of the ferrite cores on the winding [25]. Also, the gap between the ferrite cores and the shielding plates g_{fa} is considered. Due to the non-polarized field distribution of the rectangular coil, the shielding plates tend to have a considerable eddy current losses when g_{fa} is minimal. The investigation on g_{fa} could be helpful to improve the efficiency of the charging pad.

C. Multi-Objective Optimization

TABLE II
DESIGN REQUIREMENTS OF THE SYSTEM

Items	Symbol	Unit	Value
Output power	P_{out}	kW	20
Air gap distance	δ	mm	150
Operation frequency	f_{s}	kHz	85
DC voltage limit	$U_{\mathrm{dc,max}}$	V	850
Lateral misalignment	Δx	mm	150

The objectives of the optimization are to maximize the power transfer efficiency under aligned η_{al} and misaligned η_{mis} conditions, and the power density in terms of the Rx pad area ρ_{A} and total weight of the coupler ρ_{G}. The design requirements of the IPT system are listed in Table II. The air gap distance and operating frequency are selected to comply with the SAE J2954 standard [57]. For the SS compensated IPT system, when the losses in the compensation capacitors are much less than the charging pads, the maximum efficiency η_{max} of the IPT system increases when FOM becomes large as [18]

$$\eta_{\mathrm{max}} = \frac{FOM_1 FOM_2}{(1+\sqrt{1+FOM_1 FOM_2})^2} \tag{23}$$

where subscript $= 1, 2$ stands for the Tx and Rx side. Eq. (23) proves that increasing the magnetic coupling can improve the power efficiency of a IPT system. Correspondingly, the DC voltage limit has to be increased to transfer the rated power based on (15). Meanwhile, the battery voltage for electric passenger vehicles can reach above $800\,\mathrm{V}$ [54]. Therefore, the DC voltage limit is selected to be $850\,\mathrm{V}$. The lateral misalignment is set to be $150\,\mathrm{mm}$ which is larger than the recommended misalignment test value $100\,\mathrm{mm}$ in the SAE J2954 standard [57]. The design variables and their search space are listed in Table III.

TABLE III
DESIGN VARIABLES AND SEARCH SPACE

Variables	Symbol	Unit	Range
Number of turns	N	-	10-35
Number of ferrites	n_{fe}	-	5-9
Inner length	l_{in}	mm	25-300
Inner width	w_{in}	mm	25-300
Ferrite thickness	h_{fe}	mm	5-35
Ferrite width	w_{fe}	mm	15-45
Relative ferrite length	$l_{\mathrm{fe,r}}$	%	50-150
Relative gap between ferrites	$w_{\mathrm{ag,r}}$	%	10-100
Gap between coil and ferrites	g_{cf}	mm	0.1-5
Gap between ferrites and shielding	g_{fa}	mm	1-20
Gap between coil turns	g_{turn}	mm	1-3

The optimization results are presented in Fig. 10 and 11 where each point represents a unique design of the IPT system. η_{al} and η_{mis} include the power losses in the power converters, compensation capacitors and charging pads. η_{mis} is calculated when the lateral offset Δx is $150\,\mathrm{mm}$. For the SS compensated IPT system, the winding current stress increases

as the coupling declines due to the offset. The winding current density is limited below $5\mathrm{A/mm^2}$ for the thermal safety. The maximum magnetic field density in the ferrites is set to be $350\ \mathrm{mT}$ to avoid the saturation of the ferrite cores. The color of points indicates FOM of each design. A trade-off emerges between the power transfer efficiency and the power density. A trend can be seen that decreasing the power density, by increasing either the total weight or the Rx pad surface area, can improve the power transfer efficiency.

As proved by (23), $\eta_{\max}$ becomes higher as the FOM increases. Given that f_s is fixed, one of the ways to improve FOM is to increase the coil number of turn N for a higher coil quality factor Q. It is because $R_{\mathrm{dc,i}} \propto N_{\mathrm{i}}$ and $L_{\mathrm{i}} \propto N_{\mathrm{i}}^2$. This can explain why designs with lower ρ_{G} could reach a larger FOM and also a higher η_{al}, which is shown in Fig. 10(a) and 11(a). However, as Q goes high, the losses in the compensation capacitors becomes comparable with that of the charging pads. It is reported in [15] that the calculated loss in the capacitor is comparable with that in charging pads. The power loss factor $tan\delta$ of commercial film capacitor can be 0.2%. In that case, the charging pad with Q above 500 theoretically produces less power loss than the corresponding compensation capacitor. As a result, designs with high Q using more copper to gain a higher FOM cannot always guarantee a higher efficiency.

FOM can also be improved by applying more ferrite cores. As shown in Fig. 12(b), the average magnetic field density B_{avg} within the ferrite cores decreases as the weight percentage of the ferrite cores p_{fe} increases. It suggests a lower ferrite core loss density according to (17). As per Fig. 12(a), η_{al} generally increases as a higher p_{fe} is applied when M is approximately the same. On one hand, designs with a higher p_{fe} tends to have a lower B_{avg} and less amount of copper, implying a lower R_{ac}. On the other hand, the winding currents are decided by M based on (1). Thus, it is advantageous to increase the usage of ferrites to reach a large M whose feasible range is decided by the DC voltage limit as

$$M \leq \frac{8U_{\mathrm{dc,max}}^2}{\pi^2 \omega_{\mathrm{s}} P_{\mathrm{out}}} \tag{24}$$

When M is beyond the range in (24), the IPT system is incapable of delivering the rated power.

Based on the Pareto fronts in Fig. 10 and 11, a design with $\rho_{\mathrm{G}} = 0.84\ \mathrm{kW/kg}$ and $\rho_{\mathrm{A}} = 0.69\ \mathrm{kW/dm^2}$ is chosen and highlighted with a star. The highlighted design is on the Pareto fronts in Fig. 10 with a high aligned efficiency of 97.5%. Under the misaligned condition, this design delivers an efficiency of 94.1% which is close to but not on the Pareto front of Fig. 11. When comparing Fig. 10 and 11, the maximum value of FOM generally drops by half due to the decreased coupling caused by the misalignment. To improve the misalignment coupling, charging pads with a larger area and more cost of material are preferred, thus resulting in an noncompetitive FOM. Consequently, a trade-off might be made between η_{al} and η_{mis}. Since the design target is the static charging application, the misalignment between the Tx and Rx pads is commonly within a narrow range, so it is prioritized to have a high η_{al}. Besides, the size of the Rx pad

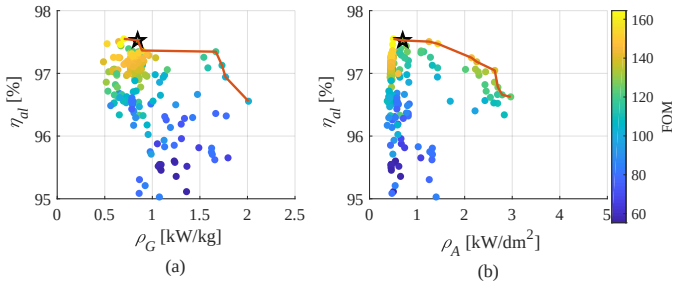

Fig. 10. Pareto optimal fronts between η_{al} and (a) ρ_{G} and (b) ρ_{A} with the color indicating the value of FOM.

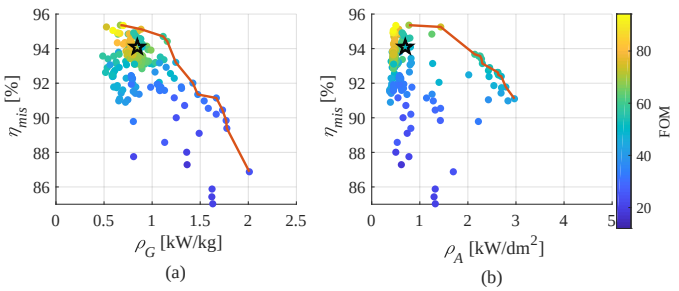

Fig. 11. Pareto optimal fronts between η_{mis} and (a) ρ_{G} and (b) ρ_{A} with the color indicating the value of FOM.

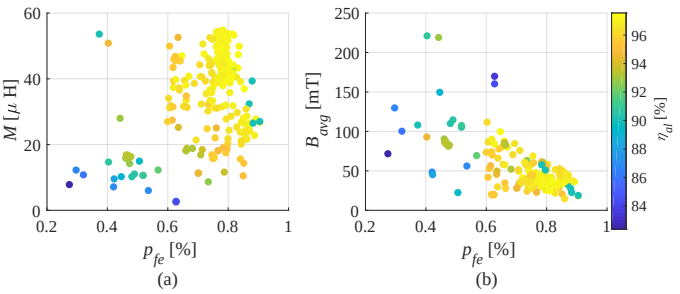

Fig. 12. Influence of p_{fe} on (a) M and (b) B_{avg} with the color indicating η_{al}.

is $544.8\mathrm{mm} * 562.7\mathrm{mm}$ which is also acceptable. Thus, the highlighted design is selected for prototyping.

VI. Experimental Validation

To verify the performance of the optimal design, an IPT system is built, consisting of the full-bridge inverter and rectifier, the compensation capacitor boards, and the Tx and Rx pads, as depicted in Fig. 13. The DC-DC power transfer efficiency is measured under the aligned and $150\ \mathrm{mm}$ lateral misalignment conditions.

A. Accuracy of FE Models

The specifications of the optimal design are illustrated in Table IV. The structure of the charging pads is presented in Fig. 13, where the copper shielding plates are removed. According to the size of the Rx pad, the prototype has an area power density of $69.1\ \mathrm{kW/m^2}$. The protective housing is made of polyoxymethylene (POM). The thickness of the bottom and wall of the POM housing is designed to be 10

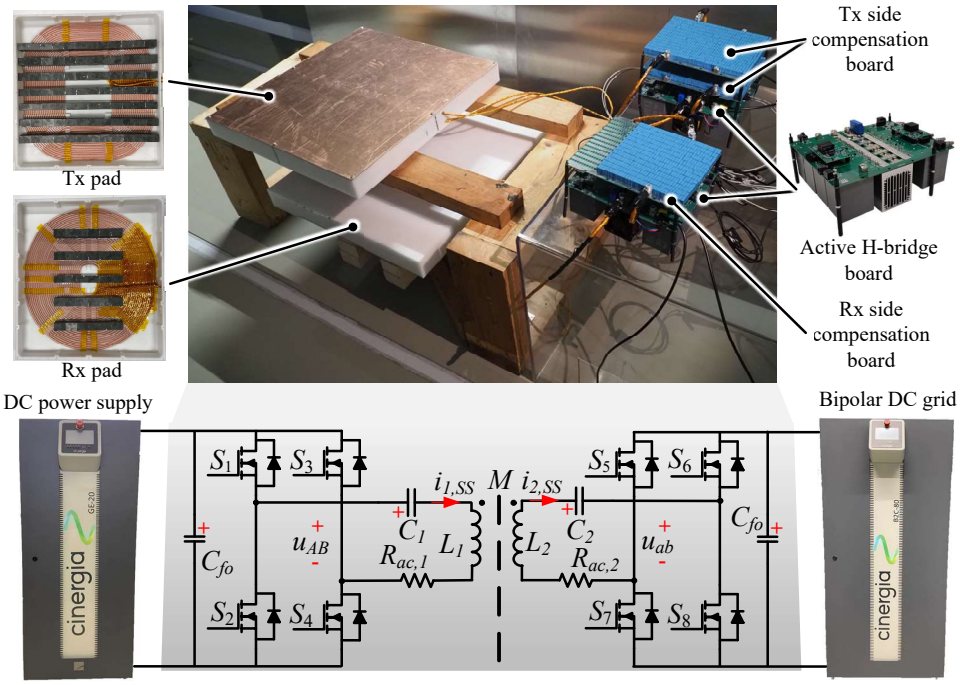

Fig. 13. Pictures and circuit schematics of the developed IPT system.

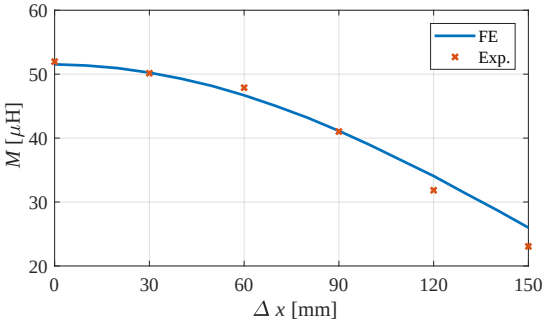

Fig. 14. Comparison of M obtained from FE models and experiments.

TABLE IV
SPECIFICATIONS OF THE SELECTED DESIGN

Variables	Symbol	Unit	Tx/Rx
Number of turns	N	-	23/31
Number of ferrites	n_{fe}	-	7/5
Inner length	l_{in}	mm	184.7/66.2
Inner width	w_{in}	mm	220.8/114.2
Ferrite thickness	h_{fe}	mm	28.8
Ferrite width	w_{fe}	mm	27.7
Ferrite length	l_{fe}	mm	515.3/243.1
Gap between ferrites	w_{ag}	mm	41.8/69.3
Gap between coil and ferrites	g_{cf}	mm	3.9/1
Gap between ferrites and shielding	g_{fa}	mm	10.6/15.0
Gap between coil turns	g_{turn}	mm	2.2

mm for a minimal deformation while supporting the weight of the litz wire and ferrite cores. To reduce the fabricating labor, channels are milled in the POM housing to guide the litz wire. The barriers of channels can improve the insulation level between adjacent coil turns and the height is used to maintain the gap between the coil and ferrite cores. The strand diameter of the litz wire is selected to be 71 μm to minimize the skin effect at 85 kHz. To limit the current density through the coils, the litz wire has 2200 strands. It is shown in Fig. 5 that the voltage stress can reach around 8 kV which is the voltage between the inner turn and the outer turn of the charging pads. Thus, a special attention is paid to the insulation of the litz wire segment stretching from the inner turn to the edge of the POM housing, and extra insulation tape is wrapped on this litz wire segment, as shown in Fig. 13. The charging pad dimension and total weight including the housing material are $516 * 552 * 60$ mm^3/25 kg for the Tx side and $514*562*60$ mm^3/21 kg for the Rx side. Correspondingly, the gravimetric and volumetric power density are 0.435 kW/kg and 581 kW/m^3, respectively.

The comparison of M between the FE models and experiments is depicted in Fig. 14. The maximum relative error is 12% and occurs at 150 mm lateral offset. Considering the possible spatial location error, the difference between the measurements and FE analysis is mostly acceptable. L_1 and L_2 are measured to be 292.3 μH and 199.6 μH, respectively. Based on the tuning method in (5) and (2), C_1 and C_2 are designed to be 11.99 nF and 17.57 nF. Each capacitor unit has 6.7 nF and 400 V rms limit. Considering the rms voltage limit of 8 kV, the capacitor boards are designed as $n_{\mathrm{s},1} = 26$, $n_{\mathrm{p},1} = 45$, $n_{\mathrm{s},2} = 13$ and $n_{\mathrm{p},2} = 34$.

B. Power Transfer Efficiency

According to the load matching method described in Section IV, the output power is regulated by changing $U_{\mathrm{dc},1}$ while $U_{\mathrm{dc},2}$ is controlled by a back-end DC-DC converter to achieve load matching for the maximum efficiency. Since the DC-DC converter design may change for EVs with different battery voltages, the DC-DC power transfer efficiency discussed in

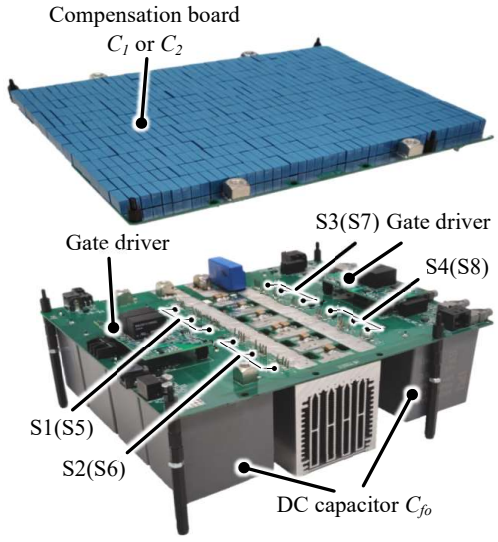

Fig. 15. Full-bridge converter with the series compensation capacitor board.

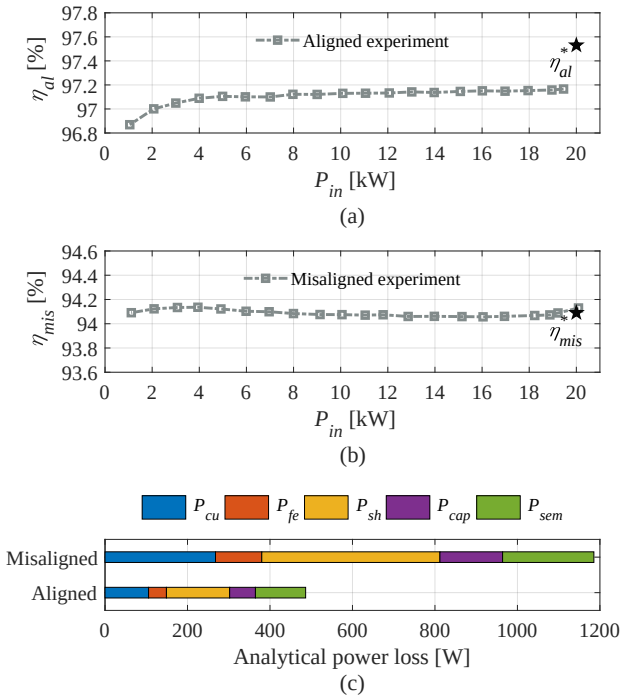

Fig. 16. Measured power transfer efficiency at different power levels under (a) aligned and (b) misaligned conditions, and (c) power losses calculated by using the proposed analytical losses model at 20 kW $P_{\rm in}$.

this paper does not include the PFC front-end circuit and back-end DC-DC converter. To test the performance of the designed prototype, the DC power supply (CINERGIA GE20) is used to provide the DC power with the voltage range of $0-750$V. The bipolar DC grid (CINERGIA B2C80) with the voltage range of $0-1500$ V and the current range of $0-41$ A is utilized as an electronic load with regenerative power injection. The DC grid is controlled to operate as a constant electronic resistor which is set to be 34 Ω and 15 Ω for the aligned and misaligned conditions, respectively.

The full-bridge converter and series compensation circuit are illustrated in Fig. 15. The Tx and Rx sides use identical full-bridge converters, but different series compensation capacitor boards. Considering the high operating frequency of 85 kHz, the commercially available SiC MOSFETs IMZ120R030M1H rated to a maximum blocking voltage of 1200 V and maximum recommended constant current of 56 A is used. At 25 °C, the on-state resistance is 30 mΩ. To reduce the conduction losses, three MOSFETs are connected in parallel for each functional switch of the full bridge converter.

By adjusting $U_{\rm dc,1}$, the power transfer efficiency with $P_{\rm in}$ ranging from $1-20$ kW is presented in Fig. 16(a) and 16(b). The DC-DC power transfer efficiency is measured by a power analyser (YOKOGAWA WT500). As shown in Fig. 16(a), $\eta_{\rm al}$ increases from 96.9% to 97.2% as $P_{\rm in}$ increases from 1kW to 20 kW. The designed aligned efficiency $\eta^*_{\rm al}$ is 97.5% which is just 0.3% higher than the measurement at 20kW. The power transfer efficiency under misaligned condition is shown in Fig. 16(b), where $\eta_{\rm mis}$ fluctuates in a small range. At the rated operation condition, $\eta_{\rm mis}$ is 94.1% which is almost equal to the designed value $\eta^*_{\rm mis}$. The analytical power losses of different components at 20 kW $P_{\rm in}$ is depicted in Fig. 16(c). The major part of the power losses is $P_{\rm sh}$, followed by $P_{\rm cu}$ and $P_{\rm sem}$.

The measured waveforms and power transfer efficiency at the rated power are illustrated in Fig. 17. It can be seen in both Fig. 17(a) and 17(c) that $u_{\rm AB}$ leads i_1 by a certain degree, thus ensuring the ZVS operation of the full-bridge inverter. It should be noticed that the angle of the input impedance is larger in Fig. 17(c), because L_1 increases slightly from 292.3 μH to 300.7 μH due to the misalignment.

VII. Conclusion

This paper has presented the detailed design guideline and demonstration of a highly efficient 20 kW IPT system. The developed prototype has a higher efficiency under the aligned and misaligned condition than the 20kW+ IPT systems used for the charging of EVs in the IEEE literature. To provide a clear guideline on the system design, the analysis and selection of the compensation circuits, and the optimization of the charging pads are detailed. A general analytical method is proposed to compare the maximum efficiency, winding current stress, capacitor voltage stress and misalignment tolerance of the SS and DLCC compensation circuits. The SS compensation is found to be more advantageous for a higher efficiency and a lower Rx side voltage and current stresses than the DLCC compensation, which is favorable in EVs charging applications. To find the optimal design of the charging pads, a MOO design method is presented. The MOO design involves both the analytical and FE models to calculate the power losses of the IPT system. Taking the aligned/misaligned efficiency and area/gravimetric power density as the objectives, the optimal Pareto fronts are obtained, and a design theoretically delivering an aligned efficiency of 97.5% and a misaligned efficiency of 94.1% is selected for prototyping. Finally, a prototype with an area power density of 69.1 kW/m^2 is built. The efficiency is measured to be 97.2% at the aligned condition and 94.1% at the misaligned condition.

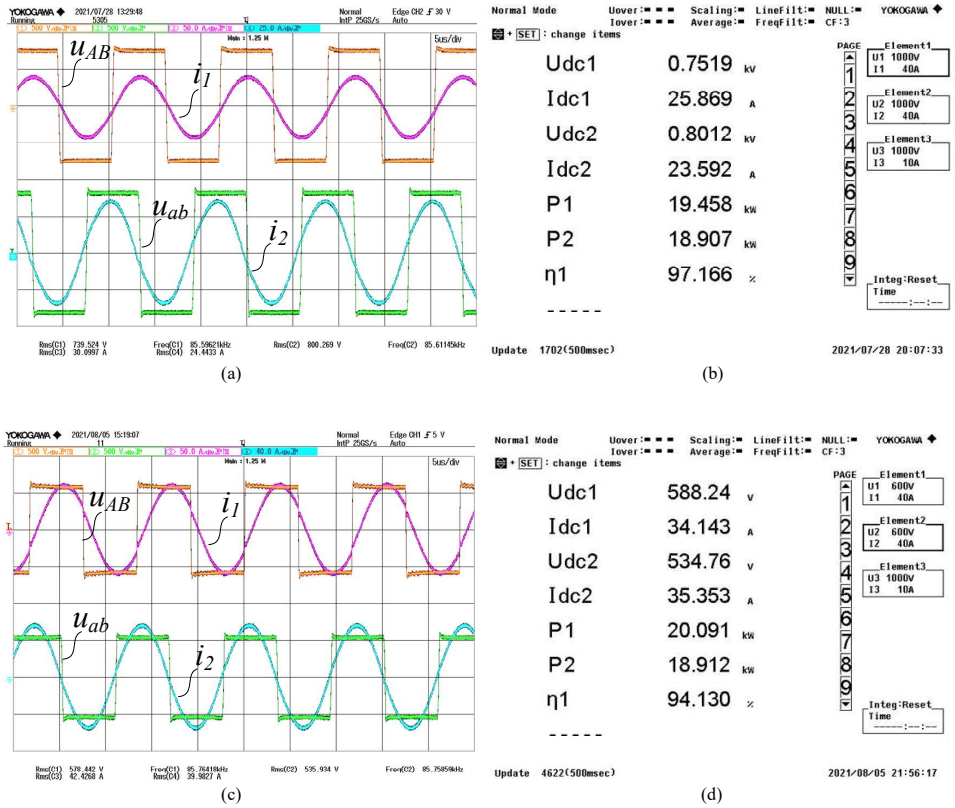

Fig. 17. Measured waveforms and power transfer efficiency at the rated power under (a) and (b) aligned, (c) and (d) misaligned conditions.

REFERENCES

[1] S. Li, S. Lu, and C. C. Mi, "Revolution of Electric Vehicle Charging Technologies Accelerated by Wide Bandgap Devices," *Proceedings of the IEEE*, vol. 109, no. 6, pp. 985–1003, Jun. 2021.

[2] G. A. Covic, J. T. Boys, M. L. G. Kissin, and H. G. Lu, "A Three-Phase Inductive Power Transfer System for Roadway-Powered Vehicles," *IEEE Transactions on Industrial Electronics*, vol. 54, no. 6, pp. 3370–3378, Dec. 2007.

[3] M. Budhia, J. T. Boys, G. A. Covic, and C. Huang, "Development of a Single-Sided Flux Magnetic Coupler for Electric Vehicle IPT Charging Systems," *IEEE Transactions on Industrial Electronics*, vol. 60, no. 1, pp. 318–328, Jan. 2013.

[4] S. Li, W. Li, J. Deng, T. D. Nguyen, and C. C. Mi, "A Double-Sided LCC Compensation Network and Its Tuning Method for Wireless Power Transfer," *IEEE Transactions on Vehicular Technology*, vol. 64, no. 6, pp. 2261–2273, Jun. 2015.

[5] J. M. Miller, P. T. Jones, J. Li, and O. C. Onar, "ORNL Experience and Challenges Facing Dynamic Wireless Power Charging of EV's," *IEEE Circuits and Systems Magazine*, vol. 15, no. 2, pp. 40–53, Secondquarter 2015.

[6] J. Huh, S. W. Lee, W. Y. Lee, G. H. Cho, and C. T. Rim, "Narrow-Width Inductive Power Transfer System for Online Electrical Vehicles," *IEEE Transactions on Power Electronics*, vol. 26, no. 12, pp. 3666–3679, Dec. 2011.

[7] J. Deng, B. Pang, W. Shi, and Z. Wang, "A new integration method with minimized extra coupling effects using inductor and capacitor series-parallel compensation for wireless EV charger," *Applied Energy*, vol. 207, pp. 405–416, Dec. 2017.

[8] W. Shi, J. Dong, T. B. Soeiro, and P. Bauer, "Integrated Solution for Electric Vehicle and Foreign Object Detection in the Application of Dynamic Inductive Power Transfer," *IEEE Transactions on Vehicular Technology*, pp. 1–1, 2021.

[9] S. Cui, Z. Wang, S. Han, C. Zhu, and C. C. Chan, "Analysis and Design of Multiphase Receiver with Reduction of Output Fluctuation for EV Dynamic Wireless Charging System," *IEEE Transactions on Power Electronics*, pp. 1–1, 2018.

[10] Z. Zhou, L. Zhang, Z. Liu, Q. Chen, R. Long, and H. Su, "Model Predictive Control for the Receiving-Side DC–DC Converter of Dynamic Wireless Power Transfer," *IEEE Transactions on Power Electronics*, vol. 35, no. 9, pp. 8985–8997, Sep. 2020.

[11] W. Shi, F. Grazian, S. Bandyopadhyay, J. Dong, T. B. Soeiro, and P. Bauer, "Analysis of Dynamic Charging Performances of Optimized Inductive Power Transfer Couplers," in *2021 IEEE 19th International Power Electronics and Motion Control Conference (PEMC)*, Apr. 2021, pp. 751–756.

[12] R. Bosshard and J. W. Kolar, "Multi-Objective Optimization of 50 kW/85 kHz IPT System for Public Transport," *IEEE Journal of Emerging and Selected Topics in Power Electronics*, vol. 4, no. 4, pp. 1370–1382, Dec. 2016.

[13] W. Li, H. Zhao, J. Deng, S. Li, and C. C. Mi, "Comparison Study on SS and Double-Sided LCC Compensation Topologies for EV/PHEV Wireless Chargers," *IEEE Transactions on Vehicular Technology*, vol. 65, no. 6, pp. 4429–4439, Jun. 2016.

[14] F. Grazian, W. Shi, T. B. Soeiro, J. Dong, P. van Duijsen, and P. Bauer, "Compensation Network for a 7.7 kW Wireless Charging System that Uses Standardized Coils," in *2020 IEEE International Symposium on Circuits and Systems (ISCAS)*, Oct. 2020, pp. 1–5.

[15] R. Bosshard, J. W. Kolar, J. Mühlethaler, I. Stevanović, B. Wunsch, and F. Canales, "Modeling and$\eta $-$\alpha $-Pareto Optimization of Inductive Power Transfer Coils for Electric Vehicles," *IEEE Journal of Emerging and Selected Topics in Power Electronics*, vol. 3, no. 1, pp. 50–64, Mar. 2015.

[16] Y. Chen, H. Zhang, C.-S. Shin, C.-H. Jo, S.-J. Park, and D.-H. Kim, "An Efficiency Optimization-Based Asymmetric Tuning Method of Double-Sided LCC Compensated WPT System for Electric Vehicles," *IEEE Transactions on Power Electronics*, vol. 35, no. 11, pp. 11 475–11 487, Nov. 2020.

[17] R. Bosshard, J. Mühlethaler, J. W. Kolar, and I. Stevanović, "The η-α-Pareto front of inductive power transfer coils," in *IECON 2012 - 38th Annual Conference on IEEE Industrial Electronics Society*, Oct. 2012, pp. 4270–4277.

[18] S. Li and C. C. Mi, "Wireless Power Transfer for Electric Vehicle Applications," *IEEE Journal of Emerging and Selected Topics in Power Electronics*, vol. 3, no. 1, pp. 4–17, Mar. 2015.

[19] M. Budhia, G. A. Covic, J. T. Boys, and C. Huang, "Development and evaluation of single sided flux couplers for contactless electric vehicle charging," in *2011 IEEE Energy Conversion Congress and Exposition*, Sep. 2011, pp. 614–621.

[20] M. Budhia, G. A. Covic, and J. T. Boys, "Design and Optimization of Circular Magnetic Structures for Lumped Inductive Power Transfer Systems," *IEEE Transactions on Power Electronics*, vol. 26, no. 11, pp. 3096–3108, Nov. 2011.

[21] A. Zaheer, D. Kacprzak, and G. A. Covic, "A bipolar receiver pad in a lumped IPT system for electric vehicle charging applications," in *2012 IEEE Energy Conversion Congress and Exposition (ECCE)*, Sep. 2012, pp. 283–290.

[22] S. Kim, G. A. Covic, and J. T. Boys, "Tripolar Pad for Inductive Power Transfer Systems for EV Charging," *IEEE Transactions on Power Electronics*, vol. 32, no. 7, pp. 5045–5057, Jul. 2017.

[23] H. Matsumoto, Y. Neba, H. Iura, D. Tsutsumi, K. Ishizaka, and R. Itoh, "Trifoliate Three-Phase Contactless Power Transformer in Case of Winding-Alignment," *IEEE Transactions on Industrial Electronics*, vol. 61, no. 1, pp. 53–62, Jan. 2014.

[24] A. Tejeda, S. Kim, F. Y. Lin, G. A. Covic, and J. T. Boys, "A Hybrid Solenoid Coupler for EV Wireless Charging Applications," *IEEE Transactions on Power Electronics*, pp. 1–1, 2018.

[25] S. Bandyopadhyay, P. Venugopal, J. Dong, and P. Bauer, "Comparison of Magnetic Couplers for IPT-Based EV Charging Using Multi-Objective Optimization," *IEEE Transactions on Vehicular Technology*, vol. 68, no. 6, pp. 5416–5429, Jun. 2019.

[26] M. Lu and K. D. T. Ngo, "A Fast Method to Optimize Efficiency and Stray Magnetic Field for Inductive-Power-Transfer Coils Using Lumped-Loops Model," *IEEE Transactions on Power Electronics*, vol. 33, no. 4, pp. 3065–3075, Apr. 2018.

[27] R. Bosshard, U. Iruretagoyena, and J. W. Kolar, "Comprehensive Evaluation of Rectangular and Double-D Coil Geometry for 50 kW/85 kHz IPT System," *IEEE Journal of Emerging and Selected Topics in Power Electronics*, vol. 4, no. 4, pp. 1406–1415, Dec. 2016.

[28] J. H. Kim, B.-S. Lee, J.-H. Lee, S.-H. Lee, C.-B. Park, S.-M. Jung, S.-G. Lee, K.-P. Yi, and J. Baek, "Development of 1-MW Inductive Power Transfer System for a High-Speed Train," *IEEE Transactions on Industrial Electronics*, vol. 62, no. 10, pp. 6242–6250, Oct. 2015.

[29] R. Bosshard, "Multi-Objective Optimization of Inductive Power Transfer Systems for EV Charging," Ph.D. dissertation, ETH Zurich, 2015.

[30] S.-H. Lee, B.-S. Lee, and J.-H. Lee, "A New Design Methodology for a 300-kW, Low Flux Density, Large Air Gap, Online Wireless Power Transfer System," *IEEE Transactions on Industry Applications*, vol. 52, no. 5, pp. 4234–4242, Sep. 2016.

[31] J. Shin, S. Shin, Y. Kim, S. Ahn, S. Lee, G. Jung, S.-J. Jeon, and D.-H. Cho, "Design and Implementation of Shaped Magnetic-Resonance-Based Wireless Power Transfer System for Roadway-Powered Moving Electric Vehicles," *IEEE Transactions on Industrial Electronics*, vol. 61, no. 3, pp. 1179–1192, Mar. 2014.

[32] R. Bosshard and J. W. Kolar, "All-SiC 9.5 kW/dm3 On-Board Power Electronics for 50 kW/85 kHz Automotive IPT System," *IEEE Journal of Emerging and Selected Topics in Power Electronics*, vol. 5, no. 1, pp. 419–431, Mar. 2017.

[33] J. Pries, V. P. N. Galigekere, O. C. Onar, and G.-J. Su, "A 50-kW Three-Phase Wireless Power Transfer System Using Bipolar Windings and Series Resonant Networks for Rotating Magnetic Fields," *IEEE Transactions on Power Electronics*, vol. 35, no. 5, pp. 4500–4517, May 2020.

[34] A. U. Ibrahim, W. Zhong, and M. D. Xu, "A 50-kW Three-Channel Wireless Power Transfer System With Low Stray Magnetic Field," *IEEE Transactions on Power Electronics*, vol. 36, no. 9, pp. 9941–9954, Sep. 2021.

[35] H. H. Wu and M. P. Masquelier, "An overview of a 50kW inductive charging system for electric buses," in *2015 IEEE Transportation Electrification Conference and Expo (ITEC)*, Jun. 2015, pp. 1–4.

[36] N. Shinohara, "Wireless power transmission progress for electric vehicle in Japan," in *2013 IEEE Radio and Wireless Symposium*, Jan. 2013, pp. 109–111.

[37] C. C. Mi, G. Buja, S. Y. Choi, and C. T. Rim, "Modern Advances in Wireless Power Transfer Systems for Roadway Powered Electric Vehicles," *IEEE Transactions on Industrial Electronics*, vol. 63, no. 10, pp. 6533–6545, Oct. 2016.

[38] A. Foote and O. C. Onar, "A review of high-power wireless power transfer," in *2017 IEEE Transportation Electrification Conference and Expo (ITEC)*, Jun. 2017, pp. 234–240.

[39] M. Bojarski, E. Asa, K. Colak, and D. Czarkowski, "A 25 kW industrial prototype wireless electric vehicle charger," in *2016 IEEE Applied Power Electronics Conference and Exposition (APEC)*, Mar. 2016, pp. 1756–1761.

[40] S. Y. Choi, S. Y. Jeong, B. W. Gu, G. C. Lim, and C. T. Rim, "Ultraslim S-Type Power Supply Rails for Roadway-Powered Electric Vehicles," *IEEE Transactions on Power Electronics*, vol. 30, no. 11, pp. 6456–6468, Nov. 2015.

[41] B. Goeldi, J. Tritschler, and S. Reichert, "Measurement Results of a 22 kW Bidirectional Inductive Charger," in *Proceedings of PCIM Europe 2015; International Exhibition and Conference for Power Electronics, Intelligent Motion, Renewable Energy and Energy Management*, May 2015, pp. 1–8.

[42] M. Mohammad, O. C. Onar, G.-J. Su, J. Pries, V. P. Galigekere, S. Anwar, E. Asa, J. Wilkins, R. Wiles, C. P. White, and L. E. Seiber, "Bidirectional LCC-LCC Compensated 20 kW Wireless Power Transfer System for Medium-Duty Vehicle Charging," *IEEE Transactions on Transportation Electrification*, pp. 1–1, 2021.

[43] S. Y. Choi, B. W. Gu, S. Y. Jeong, and C. T. Rim, "Advances in Wireless Power Transfer Systems for Roadway-Powered Electric Vehicles," *IEEE Journal of Emerging and Selected Topics in Power Electronics*, vol. 3, no. 1, pp. 18–36, Mar. 2015.

[44] T. Diekhans and R. W. D. Doncker, "A Dual-Side Controlled Inductive Power Transfer System Optimized for Large Coupling Factor Variations and Partial Load," *IEEE Transactions on Power Electronics*, vol. 30, no. 11, pp. 6320–6328, Nov. 2015.

[45] W. Zhong and S. Y. R. Hui, "Maximum Energy Efficiency Operation of Series-Series Resonant Wireless Power Transfer Systems Using On-Off Keying Modulation," *IEEE Transactions on Power Electronics*, vol. 33, no. 4, pp. 3595–3603, Apr. 2018.

[46] S. Li and C. C. Mi, "Wireless Power Transfer for Electric Vehicle Applications," *IEEE Journal of Emerging and Selected Topics in Power Electronics*, vol. 3, no. 1, pp. 4–17, Mar. 2015.

[47] W. Zhang, S. Wong, C. K. Tse, and Q. Chen, "Design for Efficiency Optimization and Voltage Controllability of Series–Series Compensated Inductive Power Transfer Systems," *IEEE Transactions on Power Electronics*, vol. 29, no. 1, pp. 191–200, Jan. 2014.

[48] K. Takeda and T. Koseki, "Analytical Investigation on Asymmetric LCC Compensation Circuit for Trade-off between High Efficiency and Power," in *2018 International Power Electronics Conference (IPEC-Niigata 2018 -ECCE Asia)*, May 2018, pp. 2309–2316.

[49] V.-T. Nguyen, V.-B. Vu, G. Gohil, and B. Fahimi, "Efficiency optimization of double-sided LCC topology for inductive power transfer systems," in *2021 IEEE Applied Power Electronics Conference and Exposition (APEC)*, Jun. 2021, pp. 1610–1617.

[50] W. Zhang and C. C. Mi, "Compensation Topologies of High-Power Wireless Power Transfer Systems," *IEEE Transactions on Vehicular Technology*, vol. 65, no. 6, pp. 4768–4778, Jun. 2016.

[51] C. Park, S. Lee, S. Y. Jeong, G. Cho, and C. T. Rim, "Uniform Power I-Type Inductive Power Transfer System With DQ-Power Supply Rails for On-Line Electric Vehicles," *IEEE Transactions on Power Electronics*, vol. 30, no. 11, pp. 6446–6455, Nov. 2015.

[52] A. Berger, M. Agostinelli, S. Vesti, J. A. Oliver, J. A. Cobos, and M. Huemer, "A Wireless Charging System Applying Phase-Shift and Amplitude Control to Maximize Efficiency and Extractable Power," *IEEE Transactions on Power Electronics*, vol. 30, no. 11, pp. 6338–6348, Nov. 2015.

[53] D. Pehrman, Y. Liu, C. Cui, and X. Huang, "Loss Reduction by Synchronous Rectification in a 50 kW SiC-based Inductive Power Transfer System," in *IECON 2020 The 46th Annual Conference of the IEEE Industrial Electronics Society*, Oct. 2020, pp. 3907–3912.

[54] C. Jung, "Power Up with 800-V Systems: The benefits of upgrading voltage power for battery-electric passenger vehicles," *IEEE Electrification Magazine*, vol. 5, no. 1, pp. 53–58, Mar. 2017.

[55] J. Deng, Y. Zhang, S. Wang, Z. Wang, and Y. Yang, "The Design and Coupler Optimization of a Single-Transmitter Coupled Multi-Receiver Inductive Power Transfer System for Maglev Trains," *IEEE Transactions on Transportation Electrification*, pp. 1–1, 2021.

[56] J. Mühlethaler, "Modeling and multi-objective ptimization of inductive power components," Ph.D. dissertation, ETH Zurich, 2012.

[57] F. Grazian, W. Shi, J. Dong, P. van Duijsen, T. B. Soeiro, and P. Bauer, "Survey on Standards and Regulations for Wireless Charging of Electric Vehicles," in *2019 AEIT International Conference of Electrical and Electronic Technologies for Automotive (AEIT AUTOMOTIVE)*, Jul. 2019, pp. 1–5.

Wenli Shi received the B.S. degree in automotive engineering from Jilin University, China, in 2015, and the M.S. degree in mechanical engineering from Beijing Insititue of Technology, China, in 2018. He is currently working towards the Ph.D. degree in the field of dynamic wireless charging of electric vehicles at the DC System, Energy Conversion and Storage (DCE&S) group, Delft University of Technology (TU Delft), The Netherlands. His research interests include foreign object detection, multi-objectives optimization design, dynamic modeling and control for wireless power transfer.

Jianning Dong received his B.S. and Ph.D. degrees in electrical engineering from Southeast University, Nanjing, China, in 2010 and 2015, respectively. Since 2016, he has been an Assistant Professor at the DC System, Energy Conversion and Storage (DCE&S) group, Delft University of Technology (TU Delft), Delft, The Netherlands. Before joining TU Delft, he was a Postdoctoral Researcher at McMaster Automotive Resource Centre, McMaster University, Hamilton, ON, Canada. His research interests include electromechanical energy conversion and contactless power transfer.

Thiago Batista Soeiro received the B.Sc. (Hons.) and M.Sc. degrees in electrical engineering from the Federal University of Santa Catarina, Florianopolis, Brazil, in 2004 and 2007, respectively, and the Ph.D. degree from the Swiss Federal Institute of Technology, Zurich, Switzerland, in 2012.

During the Master and Ph.D. studies, he was a visiting scholar at the Power Electronics and Energy Research Group, Concordia University, Montreal, QC, Canada, and at the Center for Power Electronics Systems, Blacksburg, VA, USA, respectively. From 2012 to 2013, he was a Researcher at the Power Electronics Institute, Federal University of Santa Catarina. From October 2013 to April 2018, he worked initially as a Scientist and later as a Senior Scientist at the Corporate Research Center, ABB Switzerland Ltd., Baden-Dattwil, Switzerland. Since May 2018, he has been working at the DC Systems, Energy Conversion and Storage Group, Delft University of Technology, Delft, The Netherlands. He is currently an Associate Professor and his research interests include advanced high power converters and dc system integration.

Dr. Soeiro was a recipient of the 2013 IEEE Industrial Electronics Society Best Conference Paper Award and the Best Paper Awards in the following IEEE conferences: International Conference on Power Electronics (ECCE Asia 2011), International Conference on Industrial Technology (ICIT 2013), Conference on Power Electronics and Applications EPE'15 (ECCE Europe 2015), and 19th International Power Electronics and Motion Control Conference (PEMC 2020).

Calvin Riekerk received the B.S. degree and M.S. degree in electrical engineering from the Delft University of Technology (TU Delft), The Netherlands in 2018 and 2020. Currently, he is working towards a Ph.D. degree at the DC System, Energy Conversion and Storage (DCE&S) group, TU Delft. His research interest is in wireless power transfer.

Francesca Grazian received her Bachelor degree in Electrical Engineering from the University of Bologna, Italy, in 2016. After this, she received her Master's degree in Electrical Engineering from the Delft University of Technology in 2018, focusing on Power Electronics. Her research interest in wireless power transfer begins from her Master Thesis, and she is currently developing it further as a Ph.D. candidate at the Delft University of Technology.

Guangyao Yu received the bachelor's degree in electrical engineering from Zhejiang University in 2015 and master's degree (Cum Laude) in electrical engineering from Delft University of Technology in 2020. Now he is working at TU Delft as a PhD student, his research interest is power electronics.

Pavol Bauer received master's degree in electrical engineering from the Technical University of Kosice, Kosice, Slovakia, in 1985 and the Ph.D. degree from the Delft University of Technology, Delft, The Netherlands, in 1995.

He is currently a full Professor with the Department of Electrical Sustainable Energy 0f Delft University of Technology and head of DC Systems, Energy Conversion and Storage group. He received Masters in Electrical Engineering at the Technical University of Kosice ('85), Ph.D. from Delft University of Technology ('95) and title prof. from the president of Czech Republic at the Brno University of Technology (2008) and Delft University of Technology (2016). He is also honorary professor at Politehnica University Timisioira in Romania. From 2002 to 2003 he was working partially at KEMA (DNV GL, Arnhem) on different projects related to power electronics applications in power systems. He published over 95 journal and 350 conference papers in his field (with H factor Google scholar 39, Web of Science 29), he is an author or co-author of 8 books, holds 9 international patents and organized several tutorials at the international conferences. He has worked on many projects for industry concerning wind and wave energy, power electronic applications for power systems such as Smarttrafo; HVDC systems, projects for smart cities such as PV charging of electric vehicles, PV and storage integration, contactless charging; and he participated in several Leonardo da Vinci, H2020 and Electric Mobility Europe EU projects as project partner (ELINA, INETELE, E-Pragmatic, Micact, Trolly 2.0, OSCD) and coordinator (PEMCWebLab.com-Edipe, SustEner, Eranet DCMICRO). He is a Senior Member of the IEEE ('97), former chairman of Benelux IEEE Joint Industry Applications Society, Power Electronics and Power Engineering Society chapter, chairman of the Power Electronics and Motion Control (PEMC) council, member of the Executive Committee of European Power Electronics Association (EPE) and also member of international steering committee at numerous conferences.